accepted for publication in the Astronomical Journal (AJ)
Preprint typeset using LaTeX style emulateapj v. 14/09/00

EVIDENCE FOR BLOW–OUT IN THE LOW–MASS DWARF GALAXY HOLMBERG I

Jürgen Ott[1]
Radioastronomisches Institut der Universität Bonn, Auf dem Hügel 71, 53121 Bonn, Germany
jott@astro.uni-bonn.de
Fabian Walter[1]
California Institute of Technology, Owens Valley Radio Observatory, Astronomy Department 105–24, Pasadena, CA 91125, USA
fw@astro.caltech.edu
Elias Brinks
Departamento de Astronomía, Universidad de Guanajuato, Apartado Postal 144, Guanajuato, Gto 36000, Mexico
ebrinks@astro.ugto.mx
Schuyler D. Van Dyk
Infrared Processing and Analysis Center/California Institute of Technology, Mail Code 100–22, Pasadena, CA 91125, USA
vandyk@ipac.caltech.edu
Boris Dirsch
Universidad de Concepción, Departamento de Física, Casilla 160–C, Concepción, Chile
bdirsch@cepheid.cfm.udec.cl
and
Ulrich Klein
Radioastronomisches Institut der Universität Bonn, Auf dem Hügel 71, 53121 Bonn, Germany
uklein@astro.uni-bonn.de
accepted for publication in the Astronomical Journal (AJ)

ABSTRACT

We present radio and optical observations of Holmberg I (Ho I), a member of the M 81 group of galaxies (distance ~ 3.6 Mpc). Ho I is a low–mass, low surface–brightness dwarf galaxy. High–resolution multi–array Very Large Array observations in the line of neutral hydrogen (H I) reveal a supergiant shell (diameter 1.7 kpc) which covers about half the optical extent of Ho I and which comprises 75% of the total H I content (total H I mass: $1.1 \times 10^8\,\mathcal{M}_\odot$). We estimate the scaleheight of the H I layer to be $250\,\mathrm{pc} \lesssim h \lesssim 550\,\mathrm{pc}$. We set a tentative upper limit to the dark matter content of $\lesssim 3.1 \times 10^8\,\mathcal{M}_\odot$. The H I data are complemented by deep, optical UBV(RI)$_c$ observations and narrow band Hα imaging obtained at the Calar Alto 2.2 m telescope. We find $\mathcal{M}_{\rm HI}/L_{\rm B} = 1.1\,\mathcal{M}_\odot/L_{\rm B_\odot}$. The total visible (stars plus gas) mass of Ho I adds up to $2.4 \times 10^8\,\mathcal{M}_\odot$. This leads to a total mass of $\lesssim 5.5 \times 10^8\,\mathcal{M}_\odot$ and an inclination for Ho I of $10^\circ \lesssim i \lesssim 14^\circ$.

The origin of Ho I's peculiar H I morphology is discussed in terms of a supergiant shell created by strong stellar winds and supernova explosions. We estimate that the energy deposited falls in the range of $1.2 \times 10^{53}\,\mathrm{erg} \lesssim E \lesssim 2.6 \times 10^{53}\,\mathrm{erg}$ (equivalent to 120–260 type II SN explosions). From a comparison with isochrones as well as from dynamical modeling based on the H I data we derive an age for the supergiant H I shell of $\sim 80 \pm 20$ Myr. The morphological center of Ho I (i.e., the center of the ring) is offset by 0.75 kpc with respect to the dynamical center. Within the interior of the shell the light distribution is exponential with a rather shallow gradient and blue optical colors. Beyond a radius corresponding to an H I column density of $\sim 10^{21}\,\mathrm{cm}^{-2}$, the putative star formation threshold, the disk becomes considerably redder and the slope for the exponential light distributions steepens. We attribute this to a uniform star formation activity in the recent past within the central 2 kpc of Ho I. Color–magnitude diagrams based on our CCD data show that the youngest stars, with ages of 15–30 Myr, are situated along the inside of the rim of the giant H I shell which is where we also find some faint H II regions. It is speculated that these stars are the result of secondary star formation on the rim of the shell. Based on the global morphology and velocity dispersion as well as the location of the H II regions we find evidence for ram pressure within the M 81 group. Finally, we discuss the likelihood of Ho I having lost some of its interstellar material to the intergalactic medium ("blow–out" scenario).

Subject headings: galaxies: individual (Holmberg I, UGC 5139, DDO 63) — galaxies: irregular — galaxies: dwarf — galaxies: photometry — ISM: bubbles — ISM: HI

1. INTRODUCTION

Star formation (SF), and subsequent evolution of the most massive stars, is believed to play a dominant role in shaping the interstellar medium (ISM) of galaxies. Stars with masses larger than $8\,\mathcal{M}_\odot$ first produce wind–blown bubbles within which core–collapse supernovae (SNe) oc-

[1] Visiting Astronomer, German–Spanish Astronomical Centre, Calar Alto, operated by the Max–Planck–Institute for Astronomy, Heidelberg, jointly with the Spanish National Commission for Astronomy.

cur, typically on time scales of $0.3 - 4 \times 10^7$ years (Leitherer et al. 1999). Each of these type II SNe releases a total energy of $\sim (2-3) \times 10^{53}$ erg, mostly in the form of neutrinos of all flavors (for a review see Burrows 2000). Only about 1% ($\sim 10^{51}$ erg) of this energy is deposited as kinetic energy in the environment. It is this fraction which ultimately creates features in the ISM with typical dimensions of tens of parsecs known as "bubbles" or "shells," depending whether one concentrates on the inferred three–dimensional morphology or the observed two–dimensional shape. As SF tends to occur in associations and clusters of stars one finds that the combined effects of stellar winds and SNe of an ensemble of high–mass stars can create larger features such as "superbubbles" or "supergiant shells" with radii of up to more than 1 kpc. Recent models of an evolving young association with a total stellar mass of $10^4\,\mathcal{M}_\odot$ predict a total kinetic energy input of $\sim 10^{53}$ erg (Leitherer et al. 1999). Once no further energy input is provided, i.e., after the lowest mass stars which end their lives as supernovae have disappeared, the expansion velocity of the SN–driven bubbles and shells will decrease to values similar to the velocity dispersion of the surrounding ISM. Eventually they will stall. This state of affairs is reached sooner for those bubbles which break–out of the disk of their host, leaving a morphology of a ring rather than a bubble.

The expanding shock front around each bubble piles up the surrounding ISM on its rim (see, e.g., the reviews by Tenorio–Tagle & Bodenheimer 1988; Brinks & Walter 1998, and references therein) and, if densities and temperatures are appropriate, new SF can occur. This process, known as "propagating star formation" (e.g., Mueller & Arnett 1976; Gerola & Seiden 1978; Elmegreen 1994), extends the time span for energy input and can lead to even larger shells, provided the bubble has not broken out of the disk. The recurrent deposition of such huge amounts of energy and their transformation into kinetic energy leads to a heating of the ISM, providing a natural energy source for the observed velocity dispersion of the (neutral) gas component.

It should be noted, though, that observational evidence for a stellar origin of superbubbles or supergiant shells is scarce. Only in very few cases are stellar clusters found within giant H I holes (Stewart & Walter 2000). In most cases these structures do not seem to host remnant stellar clusters, as was pointed out by Rhode et al. (1999).

Observationally, Heiles (1979, 1984) was the first to study the H I morphology and dynamics of bubbles and shells in the ISM of the Milky Way. This was followed by an analogous study of the ISM in M 31 by Brinks & Bajaja (1986). They found structures up to 700 pc in diameter. Considerably larger shells have been found in dwarf irregular galaxies (dIrr). This can be understood as follows: the low gravitational potential binds the ISM less tightly to the disk. As mentioned by Walter & Brinks (1999), the H I velocity dispersion is approximately the same in dwarf galaxies as in larger, spiral galaxies ($\sim 6-9\,\mathrm{km\,s^{-1}}$). Hence the scaleheight in dIrrs is larger than in spirals. This holds true in absolute as well as in relative terms. As a result, the volume density of the ISM is lower compared to grand–design spiral galaxies, resulting in a lower resistance against the kinetic energy input of SF regions. Secondly, the shells can evolve over a longer period. This is due to the larger scaleheight which delays and possibly even prevents break–out. Moreover, since dIrrs show mostly solid body rotation, there is little shear that may destroy shells once they have formed. Examples of objects which show large H I shell radii are Holmberg II (Puche et al. 1992), IC 2574 (Walter & Brinks 1999), IC 10 (Wilcots & Miller 1998), DDO 47 (Walter & Brinks 2001), NGC 6822 (de Blok & Walter 2000), and the Magellanic Clouds (Staveley–Smith et al. 1997; Kim et al. 1999).

To first order at least, a region of massive SF is oblivious to its environment, dumping the same amount of energy into the ISM whether it finds itself in a large spiral galaxy or in a dwarf. Therefore, for progressively lower overall galaxy mass, the impact of SF and its aftermath becomes proportionally more and more important. Theoretical models, e.g., by De Young & Heckman (1994), Mac Low & Ferrara (1999), and Ferrara & Tolstoy (2000), predict the loss of metal–enriched interstellar material associated with low–mass dwarf galaxies ($\mathcal{M}_{visible} \lesssim 10^9\,\mathcal{M}_\odot$) in the form of shells breaking out of the disk ("blow–out" scenario). As dIrrs are dominant in number in the universe and are considered to be the building blocks of larger galaxies in "bottom–up" scenarios of galaxy formation, this may have implications with respect to the enrichment of the intergalactic medium (IGM) at larger look–back times.

In some low–mass dwarf galaxies the ISM shows an almost perfect ring feature in H I, more or less centered on the optical galaxy. According to the models discussed above this may be indicative of a recent starburst in the center of the galaxy which created the cavity. In these galaxies, the total mass may just have been high enough to retain the expanding material. Objects with even lower mass ($\mathcal{M}_{visible} \lesssim 10^6\,\mathcal{M}_\odot$) would have suffered "blow–away" (Ferrara & Tolstoy 2000) of the entire ISM by a similar event. Examples of gaseous rings in dwarf irregular galaxies which suggest blow–out are Leo A (Young & Lo 1996), Sag DIG (Young & Lo 1997), M 81 dw A (Westpfahl & Puche 1993), Holmberg I (Ho I, Tully et al. 1978), Cas 1 (Huchtmeier, priv. comm.), and Sextans A (Skillman et al. 1988; Van Dyk, Puche, & Wong 1998).

Multiwavelength studies, as presented in this paper, are indispensable if we wish to understand these unique systems. The particular object under study here is Holmberg I (Ho I), a dwarf irregular galaxy in the nearby M 81 group of galaxies. This object was detected by Holmberg (1950) who optically searched for members of the M 81 group. Since then, relatively few papers have been dedicated to detailed studies of Ho I. Sandage & Tammann (1974) and Tikhonov et al. (1992) performed photographic photometry. Both papers concentrate on obtaining a distance measurement using the brightest stars method. Hoessel & Danielson (1984), using early CCD imaging, studied the stellar population of Ho I in the Gunn *gri* system. Radial surface brightness profiles have been obtained by Bremnes, Binggeli, & Prugniel (1998) and Makarova (1999), both of which observed Ho I in the context of larger surveys of dwarf galaxies. The luminosity and size of H II regions, as well as the metallicity of Ho I, have been studied in detail by Miller & Hodge (1994, 1996). Westerbork H I radio synthesis observations were presented by Tully et al. (1978) whereas Puche & Westpfahl (1993) presented a pre-

liminary map of the VLA data which are reported in full in this paper.

In this paper we aim to present a consistent picture of Holmberg I, dealing with the properties and evolution of the stars and gas. In particular, we investigate the possible influence of the stellar population on the overall gas morphology and the star formation history of this galaxy. In Sect. 2 we present optical and H I observations and describe the results in Sect. 3. The wealth of data is discussed in Sect. 4 and our conclusions are summarized in Sect. 5.

2. OBSERVATIONS AND DATA REDUCTION

In this paper we use radio and optical data to study the properties of the dIrr galaxy Holmberg I (Ho I, also known as UGC 5139 or DDO 63). We combine maps in the 21–cm line of atomic neutral hydrogen (H I) with UBV(RI)$_c$ and Hα observations in the optical regime in order to study the gas and the stars, respectively. As Ho I is a member of the M 81 group we assume it to be at the same distance as M 81, 3.63 ± 0.34 Mpc which corresponds to $m - M = 27.80$ mag (Freedman et al. 1994). This is not too different from a direct measurement for Ho I itself, based on the brightest stars method utilizing photographic plates (Sandage & Tammann 1974): $m - M = 27.63$ mag. However, using the same technique, Tikhonov et al. (1992) found a distance module of $m - M = 29.11$ mag, which deviates substantially from the others.

2.1. *Optical observations*

Optical images were obtained at the Calar Alto[2] 2.2–m telescope. The instrument used was a combination of the focal reducer CAFOS (f/4.2) and the CCD Site#1d. This CCD has a pixel size of $0\farcs53 \times 0\farcs53$, a readout noise of 5.06 e$^-$, and a gain of 2.3 e$^-$/ADU. The Johnson filters B, V, and the Johnson–Cousins filter R$_c$ were used with integration times of 60 min, 45 min, and 35 min respectively. These observations were performed in 1999 January under seeing conditions of $\sim 1\farcs4$. In 2000 January we completed the UBV(RI)$_c$ imaging with the U (100 min integration time) and I$_c$ (90 min) filters. The seeing was again $\sim 1\farcs4$. Unfortunately the I$_c$ exposure suffers from fringing at the $\approx 2.5\%$ level of the global sky background. This results in the loss of faint structures and a reduced limiting magnitude. Additionally, an Hα image (1999 January) with 60 min integration time was obtained. Due to the bandwidth of the filter (12 nm), this image still contains some [N II] emission. All images were bias–subtracted using an average value of the overscan region. Flatfield exposures were produced by taking the median of different skyflats of the same night. All reduction steps were performed using the IRAF[3] (Tody 1993) software package.

All observations were split into three or more exposures, allowing a straightforward elimination of cosmic ray pixels and other image defects by applying the CCD clipping algorithm CCDCLIP. Calibration was performed with ~ 15 Landolt standard stars (Landolt 1992) solving for the first–order zero point, the airmass, and color terms. Fitting of the calibration coefficients was done using the task FITPARAMS. The systematic error in the calibration is estimated to be 0.05 mag in B, V, R$_c$, and 0.1 mag in U and I$_c$.

For surface brightness measurements, notoriously bright foreground stars were replaced by a Gaussian background distribution, equal in mean and scatter to the ambient brightness. We applied a median filter of $3\farcs2$ in size in order to achieve smoothness. The data were corrected for Galactic extinction E$_{B-V}$=0.048 mag at the position of Ho I (Schlegel, Finkbeiner, & Davis 1998) which was converted to the Johnson(–Cousins) bandpasses following Cardelli, Clayton, & Mathis (1989). In the case of surface brightness measurements one is interested in diffuse emission and cannot apply the aperture used for single stars. Therefore we had to compare the total flux F_{tot} of a point source with the flux F_{aper} within the aperture used. To determine F_{tot}, we opened the aperture for several stars in steps of $0\farcs5$ and measured the corresponding flux until reaching a constant value in the limit. We assumed this limit to be F_{tot}. The difference $F_{tot} - F_{aper}$ leads to corrections of 0.06 mag in B, V, R$_c$, 0.11 in U and 0.30 in I$_c$.

Crowded field photometry was performed with DAOPHOT II (Stetson, Davis, & Crabtree 1987; Stetson 1990) as implemented in IRAF. We used DAOFIND to identify candidates of unresolved sources. Subsequently we determined a PSF magnitude by a manual selection of ~ 20 sufficiently bright point sources in the field. We rejected remaining cosmic ray pixels, slightly resolved background galaxies and image artifacts by judiciously employing the *sharpness* and χ parameters that were determined during the PSF fitting. The photometric errors of the remaining point sources are displayed in Fig. 1 (because of the residual fringing we refrained from attempting any stellar crowded field photometry in the I$_c$ band).

EDITOR: PLACE FIGURE 1 HERE.

2.2. *H I observations*

Ho I was observed with the NRAO Very Large Array[4] (VLA) in B–, C–, and D–configuration (1990 July, 1990 December, and 1991 March). The parameters of the observations are listed in Table 1. For the data reduction we used two software packages: calibration was done with AIPS[5] and imaging with MIRIAD[6] (Sault, Teuben, & Wright 1995). To visualize the data, we made extensive use of the ATNF package KARMA (Gooch 1995).

[2] The Calar Alto Observatory is operated by the Max–Planck–Institut für Astronomie (Heidelberg) jointly with the Spanish Comisión Nacional de Astronomía.

[3] IRAF is distributed by National Optical Astronomy Observatories, which are operated by the Association of Universities for Research in Astronomy, Inc., under cooperative agreement with the National Science Foundation.

[4] The Very Large Array (VLA) is a telescope of the National Radio Astronomy Observatory (NRAO) which is operated by Associated Universities, Inc., under a cooperative agreement with the National Science Foundation.

[5] The Astronomical Image Processing System (AIPS) was developed by the NRAO.

[6] MIRIAD was developed by the ATNF (Australia Telescope National Facility) which is part of the CSIRO (Commonwealth Scientific and Industrial Research Organization).

EDITOR: PLACE TABLE 1 HERE.

To start with, unreliable visibilities were flagged by visual inspection of the raw *uv*–data after which we applied flux, complex gain, and bandpass calibrations using the tasks SETJY, GETJY, CALIB and BPASS. To extract the 21 cm line emission, a linear interpolation of the continuum in the *uv*–plane was applied by taking the average of line–free channels on each side of the passband. This interpolation was subsequently subtracted from all visibilities (task UVLIN). As a final step in AIPS, the calibrated datasets from all configurations were combined with DBCON.

In the imaging process the *uv*–data were Fourier transformed using both "natural" and "uniform" weighting (task INVERT within MIRIAD). As both weighting schemes have some mutually exclusive advantages, it is desirable to find the optimum between low noise and high resolution. Therefore the visibilities were also weighted with the "robust"–weighting algorithm, as originally developed by Briggs (1995). Deconvolution of the resulting cube was subsequently performed by applying the Clark CLEAN–algorithm (Clark 1980) (tasks CLEAN and RESTOR). The "robust" data cube has a synthesized beam of $8\farcs2 \times 7\farcs0$ in size (approximately 140 pc × 120 pc) with a position angle of $-73°$ and an rms noise per channel map of 1.4 mJy beam^{-1} (equivalent to a brightness temperature of 14.8 K) which corresponds to a column density of 7×10^{19} cm^{-2}.

In order to decide which emission at a faint level is real in the data cube, we produced a "master cube" where all noise dominated positions were replaced by "blank" values. To do this, we first smoothed the data cube to 20″ and blanked out all positions where the convolved signal drops to below 2.5σ rms. Secondly, the resulting cube was examined by eye for emission in each channel map. Only regions with signal in three or more consecutive channels were considered to contain genuine emission. The same areas which were blanked in the "master cube" were blanked as well in the "robust" and "natural"–weighted cube. These blanked cubes were subsequently used for the calculation of the flux and the moment maps, i.e., the velocity–integrated H I distribution, the velocity field, and the H I velocity dispersion map (task MOMENT in MIRIAD).

The data cube thus obtained is a combination of a CLEANed image and a residual dirty image. Whereas the CLEAN–beam is well defined, the effect of the residual dirty beam on the output maps is *a priori* unknown. This makes the determination of the flux level in each channel map uncertain and a correction needs to be applied. We used the method proposed by Jörsäter & van Moorsel (1995) (see also Walter & Brinks 1999). The total flux S can be computed by determining the fluxes of the dirty data cube D, the residual cube R, and the CLEAN components convolved with the CLEAN beam C via the equation

$$S = \frac{C \times D}{D - R}. \quad (1)$$

We note that we would have overestimated our H I flux by $\sim 70\,\%$ if we had not applied this correction.

3. RESULTS

3.1. *Global Optical Properties*

Figure 2 shows a true color image of Ho I based on a combination of our UBVR$_c$ CCD frames. One can clearly discern an underlying population of red objects with superimposed large collections of blue and presumably young stars (especially towards the southern part of the galaxy).

EDITOR: PLACE FIGURE 2 HERE.

Before attempting photometry on individual stars or star clusters we determined apparent and absolute integrated magnitudes for Ho I (see Table 2). Our limiting surface brightness magnitudes are approximately 26 mag/□″ (U), 27 mag/□″ (B), 26 mag/□″ (V), 26 mag/□″ (R$_c$), and 23 mag/□″ (I$_c$).
Taking

$$L_{\rm B} = 10^{-0.4(M_{\rm B}-M_{\rm B_\odot})} L_{\rm B_\odot} \quad (2)$$

and a solar absolute blue magnitude of $M_{B_\odot} = 5.50$ mag (Lang 1992) this leads to $L_{\rm B} = 1.0 \times 10^8 L_{\rm B_\odot}$. This value is corrected for Galactic foreground extinction corresponding to E_{B-V}=0.048 mag (Schlegel et al. 1998) but not for any (unknown) internal extinction within Ho I. However, since Miller & Hodge (1996) derived a metallicity of 12+log(O/H)=7.7 (≈8% solar) and extinction is correlated with metallicity, we expect the internal extinction to be negligible.

EDITOR: PLACE TABLE 2 HERE.

3.2. *H I morphology and dynamics*

3.2.1. *H I distribution*

Fig. 3 shows the "robust" weighted H I channel maps. The beam size is indicated in the lower left–hand of each panel. It is only a few times larger than the seeing of our optical observations. The region to the north–west of the center appears in nearly all channel maps, suggesting a large velocity dispersion. The area near the central position shows virtually no emission throughout the dataset. The total H I diameter of Ho I is ~ 5.8 kpc.

EDITOR: PLACE FIGURE 3 HERE.

We used the most sensitive "natural"–weighted cube for the determination of the spectrum and the flux. The H I spectrum of Ho I is shown in Fig. 4. Its shape is remarkably well described by a Gaussian with a FWHM of 27.1 km s^{-1} and a central velocity of ~ 140 km s^{-1}. Although it is not clear, a priori, why this should be so, this was noticed earlier by Lo, Sargent, & Young (1993) who, at somewhat lower velocity resolution, found similar H I spectra in nine intrinsically faint dwarf galaxies. Stil (1999) also mentioned that dwarf galaxies with a central H I hole show a single peak in their spectra. We tried to model the H I distribution of Ho I with the task GALMOD, which is part of the software package GIPSY[7]. We started with the observed properties of Ho I. Changing parameters like the

[7] The "Groningen Image Processing System"

rotation curve and/or the H I column density distribution while keeping the inclination and the dispersion fixed, led to a bimodal H I spectrum. On the other hand, varying the dispersion and/or the inclination, and leaving the column density distribution and the rotation curve untouched, kept the Gaussian shape of the spectrum.

EDITOR: PLACE FIGURE 4 HERE.

Integrating the flux over all channels yields $36.0 \pm 4.0\,\mathrm{Jy\,km\,s^{-1}}$, corresponding to a total H I mass of $1.1 \times 10^8\,\mathcal{M}_\odot$. This result places Ho I in the intermediate to low–mass range of that found for dwarf irregular galaxies. Our values compare well with earlier single–dish measurements by Dickel & Rood (1978) who found $39.7\,\mathrm{Jy\,km\,s^{-1}}$. This indicates that we hardly miss any extended emission in our interferometric observations. Note that the value quoted by Allen & Shostak (1979) of $49.0\,\mathrm{Jy\,km\,s^{-1}}$ is off by a fairly large margin. We do not have an explanation for this difference other than possible confusion with ambient neutral (Galactic) gas within their large beam. The observed H I mass leads to an $\mathcal{M}_{\rm HI}/L_{\rm B}$ ratio of $1.1\,\mathcal{M}_\odot/L_{\rm B_\odot}$.

A prominent depletion of atomic gas is seen in the center of the integrated H I map (Fig. 5), while the bulk of the emission is found in a ring. The highest column densities, $2.0 \times 10^{21}\,\mathrm{cm^{-2}}$, are encountered towards the south–east, where the column density is marginally higher than the average value in the ring.

EDITOR: PLACE FIGURE 5 HERE.

In Fig. 6 we plot the azimuthally–averaged column density versus radius, taking the center of the ring as the origin (i.e., the position of lowest H I column density as indicated by a cross in Fig. 5). As we will explain below, this does *not* coincide with the dynamical center of the galaxy. Figure 6 shows that the ring peaks at a radius of $52''$, corresponding to a diameter of $\sim 1.7\,\mathrm{kpc}$, followed by a fairly steep decline. From a radius of $125''$ onwards the H I profile levels off. A determination of the H I mass located in the ring by integrating the radial profile down to a radius of $125''$ yields $\sim 8 \times 10^7\,\mathcal{M}_\odot$, which is nearly 75% of the total H I mass in the system (see also Sect. 4.7). The contrast in column density between the central H I depression at $\alpha_{2000} = 9^h40^m30^s$, $\delta_{2000} = 71°11'1\farcs8$ and the ring–like structure is about a factor of 20, with a central, average value of $6 \times 10^{19}\,\mathrm{cm^{-2}}$. In the following, we refer to this location of lowest column density within the ring as the morphological center and use it as the center of the ring itself. The error of this position is only given by the beam of the H I observation. However, the ring seems to be slightly elongated in the north–south direction. Judging from the rim alone, the genuine center of the ring–like structure might differ from the point of lowest column density by $\sim 10''$.

EDITOR: PLACE FIGURE 6 HERE.

3.2.2. *H I velocity field*

Fig. 7 shows the intensity–weighted velocity map of Ho I, overlaid as contours on the integrated H I map. The projected velocity contours shown span a range between $130\,\mathrm{km\,s^{-1}}$ and $150\,\mathrm{km\,s^{-1}}$, implying that Ho I is rotating. However, the irregularity of the isovelocity contours shows that turbulent motions dominate. This is confirmed by inspection of position–velocity (pV) cuts along the kinematical major and minor axis and through the center of the hole (Fig. 8). The ring, described in the previous section, is not seen to be expanding. However, this might be due to the rather face–on view of Ho I.

EDITOR: PLACE FIGURE 7 HERE.

EDITOR: PLACE FIGURE 8 HERE.

We performed a tilted–ring analysis using the H I data to derive the dynamics of Ho I. For this purpose, we smoothed the H I datacube to $20''$ resolution and used the task ROTCUR (Begeman 1989) in GIPSY. Model velocity fields were subsequently developed with the task VELFI and subtracted from the observed velocity field. This approach helps to set restrictions to the parameters determined by ROTCUR. The kinematic center as well as the systemic velocity for Ho I were found to be well constrained. The dynamical center of Ho I is located some $45''$ ($\sim 0.75\,\mathrm{kpc}$) to the north of the morphological center, at a systemic velocity of $(141.5 \pm 1)\,\mathrm{km\,s^{-1}}$. The dynamical center is indicated by the intersection of the major and minor axis in Fig. 5 at $\alpha_{2000} = 09^h40^m31\fs6$, $\delta_{2000} = 71°11'45''$. The uncertainty in determining the center is of order $5''$.

We were unfortunately not able to get stable results for the inclination (as is usually the case for nearly face–on galaxies). Not even the construction of model galaxies with the task GALMOD covering the inclination–scaleheight parameter space helped to constrain its value. The position angle was determined, within the errors, to have a constant value of 50°, measured from north through east. Rather than to plot the intrinsic rotational velocities we present in Fig. 9 a plot of $V \times \sin(i)$ as a function of radius. The rotation curve reaches a maximum near the peak of the H I ring beyond which it starts to decline. The rotation curve flattens out again for $R \gtrsim 1.5\,\mathrm{kpc}$, just where the H I ring ends. It should be borne in mind, though, that this might be an artifact due to the fact that both the position angle and inclination were kept fixed. Our results are in agreement with the earlier, low resolution data published by Tully et al. (1978).

EDITOR: PLACE FIGURE 9 HERE.

We used Fig. 9 to set an upper limit to the inclination of Ho I to $i \lesssim 14°$, by simply equating the dynamical mass to the sum of the gaseous and stellar mass, the latter one based on the optical blue luminosity (Sect. 3.1) and assuming an $\mathcal{M}_{stars}/L_{\rm B} = 1.0$. This is, of course, a lower limit for the total mass (not accounting for molecular gas and dark matter; see also Sect. 4.6).

The H I velocity dispersion shown in Fig. 10 indicates that there are two distinct regions in Ho I. In the southern part we find values of $\sim 9\,\mathrm{km\,s^{-1}}$, similar to the dispersion encountered in other quiet, gas–rich (dwarf) galaxies (see e.g., Stil 1999). In the north–western part, however,

significantly higher values of $\sim 12\,\mathrm{km\,s^{-1}}$ are found. A visual inspection of various spectra obtained at different positions reveals that the high velocity dispersion is an intrinsic property of the H I in Ho I, and not due to multiple velocity components blending along the line of sight. Table 3 summarizes the H I and optical characteristics of Ho I.

EDITOR: PLACE FIGURE 10 HERE.

EDITOR: PLACE TABLE 3 HERE.

4. DISCUSSION

4.1. *The Light Distribution*

In Fig. 11 we present the Johnson–Cousins R_c band and the Hα image, the latter one with superposed contours of the integrated H I emission. The extent of the H I is comparable to that of the underlying red low–surface brightness stellar component. The optical surface brightness distribution of the brighter component is asymmetric, being higher towards the southern half, more or less coinciding with the H I depletion. It is the same region which shows the bluest color and hence suggests a relatively young population (cf. Fig. 2). At a level of $\mu_B = 25\,\mathrm{mag}/\Box''$ (D_{25}) this population extends over $220'' \times 60''$, or $3.7\,\mathrm{kpc} \times 1\,\mathrm{kpc}$, with a position angle of $\sim 112°$.

EDITOR: PLACE FIGURE 11 HERE.

Fig. 12 shows the azimuthally–averaged UBV(RI)$_c$ surface brightness profiles of Ho I centered on the morphological center of the H I hole. As an interesting feature we note that the U, B, V, and R_c band profiles show a change in slope at about the D_{25} diameter, with a steep exponential profile at the outer parts of Ho I, and a shallower exponential disk towards the center. The difference in slope between the inner and outer parts becomes less pronounced with increasing wavelength. An elliptical averaging, following the optical isophotes, leads to a similar distribution with the kinks at the same radii.

If it were not for the absence of a bulge component, the surface brightness profile would be classified as a Type II profile (Freeman 1970). The kink is located at the outer edge of the H I ring, where the H I column density falls below the empirical SF threshold of $10^{21}\,\mathrm{cm^{-2}}$ (Skillman 1987), as indicated by the right–most dotted vertical line in Fig. 12. We disregard absorption as a possible mechanism for the change in slope. Given the low (8% solar) metallicity, dust is expected to play a modest role, if any. Besides, the effect becomes more pronounced as one moves outward which would require an increasing dust opacity with increasing radius, which is unlikely.

A more acceptable explanation is that SF has been occurring fairly uniformly within the inner $74''$ radius. Beyond this radius, current SF is suppressed (column densities are below the canonical star formation threshold). As SF has occurred recently, supposedly superimposed on an older underlying component, the light within the SF radius is still predominantly blue, hence the rather flat and blue color distribution. A similar trend has been observed in M 81 dwarf A and might therefore be a general feature of low–mass dIrr galaxies (Ott et al., in preparation).

Fig. 13 compares the azimuthally–averaged B$-$R$_c$ color with that of the Hα emission. Since the H II regions are distributed in a few patches, one should not take the averaging too literally. But it does seem significant that the Hα emission is found towards the outer edge of the H I ring. The current star formation rate (SFR) is low: Miller & Hodge (1994) derive a total Hα luminosity of $4.27 \times 10^{38}\,\mathrm{erg\ s^{-1}}$ for Ho I, which corresponds to a SFR of only $0.004\,\mathcal{M}_\odot\,\mathrm{yr^{-1}}$.

The fact that star formation is almost absent can be understood in the framework of a universal minimum surface density threshold in irregular galaxies (Gallagher & Hunter 1984; Skillman 1987; Taylor et al. 1994; van Zee, Skillman, & Salzer 1998; Hunter, Elmegreen, & van Woerden 2001). Its value hovers typically around an H I column density of $10^{21}\,\mathrm{cm^{-2}}$ which corresponds to a mass surface density of $8\,\mathcal{M}_\odot\,\mathrm{pc^{-2}}$. There is a debate going on about its exact value and its dependence on Hubble type and metallicity (e.g., Franco & Cox 1986). For larger systems, Kennicutt (1998) finds that a sample of 61 normal disk galaxies show Hα emission above a surface density of typically $\Sigma_{\mathrm{HI+H}\alpha} = 10^{0.5}\,\mathcal{M}_\odot\mathrm{pc^{-2}}$. In other words, the threshold for disk galaxies corresponds to $\sim 4 \times 10^{20}\,\mathrm{cm^{-2}}$. Inspecting Fig. 11, SF in Ho I occurs where the H I column density exceeds $\sim 9 \times 10^{20}\,\mathrm{cm^{-2}}$ or $7\,\mathcal{M}_\odot\,\mathrm{pc^{-2}}$. Hence, Ho I manages to reach values close to the empirical threshold value for dwarf galaxies in a few areas only, i.e., coinciding with the densest regions in the ring (note that in the case of dwarf galaxies one usually ignores the contributions by He or H_2 to the mass surface density).

An alternative explanation for a star formation threshold is that of gravitational instability. In gas–rich, spiral galaxies a thin gas disk will undergo gravitational collapse if its gas surface density exceeds a threshold surface density. This critical surface density is: $\Sigma_{crit} = \alpha\frac{\kappa\sigma}{3.36G}$ (Toomre 1964; Kennicutt 1989) where α is a constant of order unity, σ the 1–dimensional gas dispersion, and G is the gravitational constant; κ, the epicyclic frequency, is defined as: $\kappa = 1.41\frac{V}{R}(1 + \frac{R}{V}\frac{dR}{dV})^{1/2}$. If we consider only the H I gas parameters (cf. Tab. 3) and use the radii R and velocities V given by the rotation curve and take into account the derived inclination range at the location of the supergiant H I ring (cf. Sect. 3.2.2), we find $20\,\mathcal{M}_\odot\mathrm{pc^{-2}} \lesssim \Sigma_{crit} \lesssim 70\,\mathcal{M}_\odot\mathrm{pc^{-2}}$. The observed mass surface density never reaches more than $7\,\mathcal{M}_\odot\mathrm{pc^{-2}}$, i.e., well below what would be needed for SF to take place.

There are good reasons to argue that a thin disk approximation is not valid in the case of thick dwarf galaxies and alternative approaches are required (Hunter & Plummer 1996; Hunter, Elmegreen, & Baker 1998; Wilcots & Miller 1998; Hunter, Elmegreen, & van Woerden 2001). However, observed values for Σ_{gas}, even when corrected for He, lie comfortably below the threshold indicating that the gas disk is stable against gravitational instability and as a result does not experience large scale star formation. Both formalisms, a universal threshold and a gravitational instability criterion, seem to be able to explain the lack of current star formation in Ho I; based on the current data we find that it is not possible to decide which of the mech-

anisms is the dominant one.

EDITOR: PLACE FIGURE 12 HERE.

EDITOR: PLACE FIGURE 13 HERE.

Most of the Hα emission in Ho I lies on the outer rim of the large superbubble. This is in contrast to what has been found to be the case for the shells of, e.g., Holmberg II (Puche et al. 1992) and IC 2574 (Walter & Brinks 1999), where some of the brightest H II regions tend to coincide with the inner rims of the shells. We'd like to note that there is an obvious difference, however. In Holmberg II and IC 2574 most of the rings showing Hα emission are still expanding whereas the shell in Ho I has virtually stalled. The faint Hα seen just to the outside of the rim of Ho I's huge H I shell might thus be due to a sufficient amount of material being piled up at the front of the shell.

4.2. *Color–Magnitude Diagrams*

The seeing in our CCD images is $\sim 1\farcs4$ which corresponds to a linear resolution of 24 pc at the distance of Ho I. This means that only the largest open clusters are likely to be resolved. As a consequence, we are not able to distinguish between most of the small stellar clusters and individual stars.

To study exclusively objects belonging to Ho I it is necessary to discriminate them from unrelated foreground/background sources (Galactic stars/unresolved galaxies). This was done assuming that all sources outside a radius of $\sim 1\farcm9$, centered on the H I depression (cf. Sect. 4.1), are unrelated objects. The vast majority of these objects have colors (U−B)$\gtrsim$0.5, (B−V)$\gtrsim$0.8, and (V−R)$\gtrsim$0.6. We assume that objects with the same colors that fall within the aforementioned radius of $\sim 1\farcm9$ are background or foreground sources, too, and we exclude them from further analysis. The color–magnitude diagrams of the remaining point sources which likely belong to Ho I are shown in Fig. 14 and 15.

First, we start with assuming that all observed objects within Ho I are unresolved stellar clusters and compare their properties with the well–studied cluster population in the Large Magellanic Cloud (LMC), using the compilation of LMC clusters by Bica et al. (1996). In Fig. 14 we overlay their sample on the (U−B, B−V) color–color diagram and the (V, B−V) color–magnitude diagram (CMD) of our objects. To make a proper comparison, we adjusted the reddening of the LMC cluster compilation to the reddening towards Ho I and scaled the brightness according to the distance of Ho I. Adding up the point sources above a V magnitude of $22.2 + 1.5\,(B-V)$ — indicated by a solid line in Fig. 14 — yields a number of 40 for Ho I and 593 for the LMC. In other words, about 15 times more clusters would have been observed if the LMC were placed at the distance of Ho I. Even correcting for the fact that the LMC is a factor of 3 more gas rich than Ho I (LMC H I mass: $3.1 \times 10^8\,\mathcal{M}_\odot$, Luks & Rohlfs 1992), and scaling the number of stellar clusters with this factor, leads still to 5 times more clusters in the LMC, compared with the number of bright point sources in Ho I. The CMD of Ho I most likely consists of both stellar clusters and single stars. Therefore the cluster abundance of Ho I might be even lower. This is supported by the color–color diagram in Fig. 14, where in general the LMC clusters with (B−V)$\approx$ 0.6 are fainter in the U band compared to the point sources of Ho I.

A reason for the difference might be the ongoing interaction of the LMC with the Small Magellanic Cloud and the Milky Way. Kennicutt et al. (1987) and Bushouse (1987), for example, find an enhanced SFR in galaxies with a close companion. Ho I's neighbors, the M 81 triplet galaxies (cf. Sect. 4.5), are at a much larger projected distance for which reason the effect of tidal interactions is thought to play a less prominent role. Based on our data we can only say something about the bright and presumably rather young stellar clusters. The number of old clusters in the LMC and in Ho I might be the same, after adjusting for the sizes of the two galaxies.

EDITOR: PLACE FIGURE 14 HERE.

Second, we discuss the consequences of the assumption that all point sources are stars. We overlaid the isochrones by Bertelli et al. (1994) on the CMDs in Fig. 15. The chosen metallicity of Z=0.001 is close to the spectroscopically derived 12+log(O/H)=7.7 abundance of the brightest H II region (Miller & Hodge 1996). Note, that one cannot directly compare the metallicity given by the oxygen abundance with the heavy element abundance described by Z. For the Magellanic Clouds, however, Gilmore & Wyse (1991) find a nearly solar [O/Fe]~ -0.3. The isochrones have been reddened according to Galactic foreground extinction (Schlegel et al. 1998) in order to match the uncorrected distribution of stars in the CMDs. There is some evidence of the main sequence (MS) in all CMDs, although it is not the most populous region in the diagrams. Aparicio & Gallart (1995) found that crowding effects generally shift blue stars to the red and red stars to the blue. This finding suggests that the MS might be more populated than it appears to be in the CMDs. Together with the existence of H II regions, this is an indicator for young, not very evolved stars. However, the bulk of stars is at least older than 30 Myr ($\log t = 7.5$). In addition, we do see stars in the helium–burning (HeB) blue–loop phase. Due to the described crowding effects, the number of HeB stars might be overestimated.

EDITOR: PLACE FIGURE 15 HERE.

The filled circles in the (V, U−B) diagram indicate all stars within a radius of $0\farcm9$, well *inside* the main H I ring feature. These stars appear to follow isochrones between 15 and 30 Myr ($\log t = 7.2$–7.5), which is about half of the age derived from the H I properties of the ring (see also Sect. 4.4). All these objects are located at a mean radius of ~ 660 pc from the morphological center, following the ring–shaped H I morphology (cf. boxes in Fig. 16). The small time window supports the interpretation for the surface brightness profiles given in Sect. 4.1. If the supergiant H I shell has indeed been created by SF, part of the triggered population is most likely this population of stars.

In Fig. 16 the location of the youngest stars is shown. These stars were selected to have (U−B)$\lesssim -0.7$, (B−V)$\lesssim -0.1$, and V$\lesssim$ 23. They neither lie at the H I depression

nor at the peak of the H I ring, but rather they are associated with the currently visible H I ring. This we interpret as more evidence for the H I ring being the likely remnant of a superbubble which by its expansion has been the trigger for subsequent SF and therefore has defined the recent SF history of Ho I.

EDITOR: PLACE FIGURE 16 HERE.

In contrast, older and redder stars do not show any preferred location in Ho I. Van Dyk, Puche, & Wong (1998) found a similar behavior in the nearby dIrr Sextans A, which shows a comparable H I morphology. In Sextans A the HeB blue–loop stars are found mainly inside the H I ring–structure. Comparing the stellar photometry of Ho I with Sextans A is difficult, because Ho I is at about twice the distance. The resulting severe crowding effects can only be alleviated, e.g., by the use of space–based telescopes or adaptive optics.

4.3. *The Thickness of Ho I*

In order to set limits on the thickness of the H I layer of Ho I we proceed as follows. We assume that the H I distribution perpendicular to the disk is Gaussian–shaped; for a face–on galaxy this yields

$$N_{\rm HI} = \sqrt{2\pi}\, h\, n_{\rm HI}, \tag{3}$$

where $N_{\rm HI}$ is the H I column density, h the 1σ scaleheight and $n_{\rm HI}$ the H I particle volume density at the midplane of the disk. The equation connecting the scaleheight to the velocity dispersion is given by van der Kruit (1981):

$$h(R) = \frac{\sigma_{gas}}{\sqrt{4\,\pi\,G\,\rho_{tot}(0,R)}}. \tag{4}$$

Here, σ_{gas} is the one–dimensional H I velocity dispersion, G the universal gravitational constant, and $\rho_{tot}(0,R)$ the total mass density in the disk at radius R and $z = 0$. Using both equations we derive

$$\begin{aligned} h &= (\sqrt{8\pi}Gm_p)^{-1}\,\frac{\sigma_{gas}^2}{\frac{\rho_{tot}}{\rho_{\rm HI}}N_{\rm HI}} \\ &= 5.79\times10^{21}\left(\frac{\sigma_{gas}}{\rm km\,s^{-1}}\right)^2\left(\frac{N_{\rm HI}}{\rm cm^{-2}}\right)^{-1}\left(\frac{\rho_{\rm HI}}{\rho_{tot}}\right)\ {\rm pc}, \end{aligned} \tag{5}$$

with m_p the proton mass. For an average H I column density of $3.9\times10^{20}\,{\rm cm^{-2}}$, an average velocity dispersion of $9\,{\rm km\,s^{-1}}$, and adopting for $\rho_{tot}/\rho_{\rm HI}$ a constant ratio of 2.2 (assuming $\rho_{tot}/\rho_{\rm HI} = \mathcal{M}_{tot}/\mathcal{M}_{\rm HI}$; $\mathcal{M}_{tot} = \mathcal{M}_{\rm HI} + \mathcal{M}_{\rm He} + \mathcal{M}_{\rm stars}$, with $\mathcal{M}_{stars}/L_{\rm B} = 1$, a correction for the contribution of helium of $\mathcal{M}_{\rm He} = 0.3\mathcal{M}_{\rm HI}$ and ignoring any dark matter contribution), we derive an upper limit of $h \lesssim 550\,{\rm pc}$, corresponding to a FWHM thickness of $\lesssim 1300\,{\rm pc}$.

This is comparable to what has been found by Puche et al. (1992), Walter & Brinks (1999), and Walter & Brinks (2001) for the dIrrs Holmberg II, IC 2574, and DDO 47. From this and Eq. 3 we derive an average H I volume density of $n_{\rm HI} \gtrsim 0.10\,{\rm cm^{-3}}$ at the midplane of the disk.

4.4. *Evolution of the supergiant H I shell*

4.4.1. *Energy needed to create the shell*

As mentioned in Sect. 1, the standard scenario to explain shell structures is the deposition of vast amounts of energy via SN explosions of the most massive stars within a region of star formation, such as an OB association or a stellar cluster. Ho I shows evidence for this scenario as we see a concentration of bright, blue stars within the H I ring (see Sect. 3.1). The effect of the energy released by one SN in the post–Sedov phase on the ambient medium has been evaluated by Chevalier (1974). The kinetic energy deposited in the ISM can be derived from

$$E = 5.3\times10^{43}\left(\frac{n_0}{\rm cm^{-3}}\right)^{1.12}\left(\frac{R}{\rm pc}\right)^{3.12}\left(\frac{v}{\rm kms^{-1}}\right)^{1.40}\ {\rm erg}, \tag{6}$$

where n_0 is the volume density of the gas in the ambient medium, R the radius, and v the expansion velocity of the bubble.

It has become standard practice to take this equation and apply it to the input of an entire stellar cluster. Since we do not see the ring expanding, we can assume that the shell has more or less stalled at the radius where the expansion velocity became comparable to the H I dispersion of the ambient medium ($9\,{\rm km\,s^{-1}}$). However, due to the rather low inclination of Ho I, we cannot exclude some expansion of the supergiant shell which is not visible in the data. As volume density we take the previously calculated value for the average H I volume density of $0.10\,{\rm cm^{-3}}$ (Sect. 4.3). Based on Fig. 6 (see also Sect. 3.2.1) we derive a radius of the shell of 850 pc. This leads to an energy requirement of $\lesssim 1.2\times10^{53}\,{\rm erg}$ to create the supergiant shell, which is equivalent to the kinetic energy of ~ 120 type II SNe (this value increases by a factor of about two when taking into dark matter into account; see Sect. 4.6).

4.4.2. *Age of the shell*

We approximated the evolution of the shell by comparing it to models of a Sedov expansion phase (Sedov 1959; Mac Low & McCray 1988; Ehlerová et al. 1997). The radial evolution $R(t)$ of a supergiant shell which is driven by a SN rate $\dot{N}_{\rm SN}$ (each SN provides a kinetic energy $E_{\rm SN}$) in a medium with the particle volume density n_0 and a mean molecular mass μ is given by

$$\begin{aligned} R(t) = 53.1 &\left[\left(\frac{\dot{N}_{\rm SN}}{\rm Myr^{-1}}\right)\left(\frac{E_{\rm SN}}{10^{51}{\rm erg}}\right)\right]^{1/5}\cdot \\ &\cdot\left[\left(\frac{\mu}{1.3}\right)^{-1}\left(\frac{n_0}{\rm cm^{-3}}\right)^{-1}\right]^{1/5}\left(\frac{t}{\rm Myr}\right)^{3/5}\ {\rm pc} \end{aligned} \tag{7}$$

(note that the expansion velocity goes as $V(t) = \dot{R}(t)$).

If we assume that all of the 120 SNe (Sect. 4.4.1) went off within $4\times10^7\,{\rm Myr}$, the longest period for massive stars to exist (see, e.g., Leitherer et al. 1999), we derive an average SN rate of $3\ {\rm Myr^{-1}}$. Furthermore, we will use again a density of $0.10\,{\rm cm^{-3}}$ (Sect. 4.3), a mean molecular weight of 1.3, and an average energy of 10^{51} erg per SN. If break–out occurs, energy input into the shell becomes ineffective, and the structure enters the "snowplow" phase, i.e., an expansion with conservation of momentum. McCray &

Kafatos (1987) find that for this stage of the evolution of a supergiant shell the radius will increase as

$$R(t) = R_c \left(\frac{t}{t_c}\right)^{1/4} \quad (8)$$

beyond a critical radius R_c and a critical time t_c, which is the radius and the time of the shell right at the moment where the shell breaks out of the disk (see also Sect. 4.7). Again, the derivative of this equation yields the velocity of this phase. Fig. 17 shows the predicted radius and velocity at break–out for several critical variables. The line marked "SN driven" represents the case without break–out. The line shows the steady growth of the shell as a function of time. The labels '33,' '24,' etc., represents the expansion velocity of the shell at different ages. The family of lines marked "snowplow" represent the growth of the shell (at a lower rate) after it has broken out of the disk. Note that these calculations have been performed for a single shell with a central event. Propagating SF and simultaneous SF within the hole as suggested by the CMDs and the surface brightness distribution (Sect. 4.2 and 4.1) changes the energy and the locations of energy input and therefore the age calculations (see also Sect. 4.7).

EDITOR: PLACE FIGURE 17 HERE.

The age of the supergiant shell can be estimated using various approaches:

- An upper limit for the age of this structure can be obtained by simply dividing the radius of the shell (0.85 kpc) by the limit of the expansion velocity, $9\,\mathrm{km\,s^{-1}}$, which leads to 90 Myr.
- The dotted line in Fig. 17 shows the observed radius of the shell. Since we found the H I 1σ scaleheight to be $\lesssim 550$ pc (Sect. 4.3) we assume that the shell broke out of the disk of Ho I, a conclusion which is supported by the overall morphology (cf. Sect. 4.7). The horizontal dashed line of Fig. 17 indicates the size of the shell at blow–out. This event should have taken place at an age of ~ 15 Myr. The intersection of the current size of the shell (dotted line) with the evolutionary track of the snowplow phase (thick line) leads to a total age estimate of ~ 100 Myr.
- The stars within the H I shell of Ho I and visible in the U band are located at a mean radial distance of ~ 660 pc (the open squares in Fig. 16). This radius was achieved by the shell when it was ~ 35 Myr old (see Fig 17, the thicker drawn evolutionary track). Adding the maximum age of these stars (30 Myr, see Sect. 4.2) yields an age of ~ 65 Myr.
- If we assume that the shock front creating the ring started as an infinitesimally thin shock and assume that this shock has broadened over time, we find that for an equivalent broadening speed of $9\,\mathrm{km\,s^{-1}}$ it would take some 70 Myr to expand isotropically by 0.6 kpc (half of the FWHM of the ring).
- Comparing the integrated light of the remnant of the central cluster with the models provided by Leitherer et al. (1999) predicts, based on a surface color of $\mu_U(0) - \mu_B(0) = -0.41$, and adopting a metallicity of Z=0.001 and a Salpeter IMF, an age of ~ 60 Myr.

Given the uncertainties in each of the derived values, we conclude an age of the supergiant shell of 80 ± 20 Myr. Table 4 summarizes the properties of the H I ring.

EDITOR: PLACE TABLE 4 HERE.

4.5. *Ram pressure effects*

An obvious aspect of the global optical and H I morphology is the apparent lopsidedness. We speculate that ram pressure may play a role in causing this asymmetry, much as was proposed by Bureau & Carignan (2001) in the case of Holmberg II. If this is the case, Ho I must be falling towards the strongly interacting M 81 triplet consisting of M 81, M 82, and NGC 3077 (for a description see Yun, Ho, & Lo 1994), which lies to the south–east at a projected distance about twice the size of the triplet (distance Ho I $\leftrightarrow$ M 82: ~ 120 kpc; M 82 $\leftrightarrow$ NGC 3077: ~ 80 kpc). Ram pressure effects may have compressed the gas in the south–eastern part of Ho I, raising it above the critical level for SF. It is interesting to note in that context the main Hα emission is detected in the same south–eastern quadrant, i.e., the "leading edge" of Ho I. This is somewhat similar to what de Boer et al. (1998) found for the LMC. On the opposite side, the north–west, one would expect higher turbulence (cf. the Coma cluster; Gunn & Gott 1972). The linewidth distribution as shown in Fig. 10 corroborates this scenario. However, it may also be that the lopsided distribution of H I in Ho I is due to a (weak) tidal pull by the same M81 triplet. We consider detailed calculations of either of the two possibilities beyond the scope of this paper.

4.6. *The south–east of Ho I*

Besides the big H I hole, Ho I possesses several smaller features which are visible in the channel maps (cf. Fig. 3). The bulk of these structures are noise–dominated, so we refrain from listing all possible cavities. A prominent feature, however, is located in the south–eastern part of the ring where we find the highest H I column densities. The box marked in Fig. 5 is blown up in Fig. 18, where we show the H I, the Johnson B–band and Hα emission for comparison. This particular H I shell has a diameter of 0.5 kpc and is filled by blue stars, lending support to the picture that massive SF (and the resulting SN explosions) is shaping the surrounding ISM. The H I column density drops by a factor of ~ 3 towards the center of this ring ($N_{\rm HI} = 6 \times 10^{20}\,\mathrm{cm^{-2}}$; $\alpha_{2000} = 9^h40^m35^s$, $\delta_{2000} = 71°10'00''$). A visual inspection of pV cuts at different position angles centered on the shell, as well as various spectra in the natural weighted cube, reveals that the shell is still slightly expanding at $\sim 6.5\,\mathrm{km\,s^{-1}}$. Following Sect. 4.4 we derive for a diameter of 0.5 kpc and a density of $0.10\,\mathrm{cm^{-3}}$ an energy requirement of $E = 1.7 \times 10^{51}$ erg, corresponding to only about two supernovae. An upper limit to the age of this shell is set by the life expectancy of the

least massive star still to go off as supernova, or $40\,\mathrm{Myr}^{-1}$. If we use the same Sedov expansion phase model as in Sect. 4.4.2, we estimate for a SN rate of $0.05\,\mathrm{Myr}^{-1}$ an age of 15–20 Myr. In contrast to the location of the H II regions on the outer rim of the huge superbubble (cf. Sect. 4.1), we find Hα regions at the inside edge of the small shell, similar to what has been found for other dIrrs (Puche et al. 1992; Walter & Brinks 1999). For a velocity of $6.5\,\mathrm{km\,s}^{-1}$, the rim of the small H I shell needs some 10–15 Myr to pass a given point in space. A comparison with the derived age might then explain why the H II regions are located at the inner rim of this structure.

The detection of expansion in the z direction of the shell implies that it has not broken out of the disk yet. The scaleheight of the H I layer must therefore have a lower limit of $h \gtrsim 250\,\mathrm{pc}$, assuming an isotropic expansion. By applying Eq. 5, we find an upper limit for the total mass density of $\rho_{tot} \approx 5\rho_{\mathrm{HI}}$ within Ho I. If visible matter traces the dark matter content, we can estimate a total mass for Ho I of $\lesssim 5.5 \times 10^8\,\mathcal{M}_\odot$, which corresponds to a limit for the dark matter of $\lesssim 3.1 \times 10^8\,\mathcal{M}_\odot$. Given the relatively small amount involved, this could perhaps be accounted for by molecular gas, dust, or even a higher $\mathcal{M}_{stars}/L_{\mathrm{B}}$ ratio, in which case no dark matter would be required to explain the observed rotation curve. Adopting our curve leads to an inclination of $i \gtrsim 10°$. Employing Eq. 3 yields an upper limit for the particle volume density of $\sim 0.20\,\mathrm{cm}^{-3}$. We can now use this value to estimate an upper limit to the energy calculation of the supershell (Sect. 4.4.1): $E \lesssim 2.6 \times 10^{53}$ erg, which is equal to the energy input of about 260 SNe. The determination of the age of the shell, based on a comparison with models (cf. Sect. 4.4.2) does not change substantially; the energy depends nearly linearly on the volume density in Eq. 6. If the density doubles, the energy follows and those two factors cancel out in Eq. 7.

For the small shell, a particle volume density of $0.20\,\mathrm{cm}^{-3}$ in the disk leads to an upper limit of the energy needed for its creation of 3.6×10^{51} erg, which corresponds to about 4 SNe. Again, the estimate for its age does not change much for the reasons described above.

EDITOR: PLACE FIGURE 18 HERE.

4.7. *Blow–out*

Whether or not the central big H I hole has suffered "blow–out" (i.e., the shell breaking out of the disk *and* losing metal–enriched material to the intergalactic space) highly depends on the total mass of the galaxy. In the model of Mac Low & Ferrara (1999) and Ferrara & Tolstoy (2000), objects with visible masses below $\sim 10^9\,\mathcal{M}_\odot$ suffer blow–out. The gas would then be distributed over a bigger volume surrounding the former host. They argue that for this to work, the velocity of the expanding shells would have to exceed the escape velocity of the host galaxy. In the case of Ho I we do not see any H I along the line of sight to the central hole down to a column density of $\sim 6 \times 10^{19}\,\mathrm{cm}^{-2}$. The "line of sight" effect may contribute to the difference in the measured flux between the projected rim of a three dimensional shell and its center. This effect can, however, only account for a change of about a factor of two in column density and is insufficient to describe the observed H I gradient from the ring towards the center (a factor of ~ 20, Fig. 6).

The calculations performed in Sect. 4.4.2 and displayed in Fig. 17 suggest that the shell broke out of the disk, since the observed radius of the ring (850 pc) is considerably larger than the 1σ scaleheight of the gaseous disk ($\lesssim 550\,\mathrm{pc}$). An alternative explanation for the shell to stall is that its interior simply has cooled, reducing the overpressure. The typical timescale for such a cooling, t_{cool}, is described by McCray & Kafatos (1987):

$$t_{cool} = 4\,\zeta^{-1.5}\,(N_*\,E_{51})^{0.3}\,n_0^{-0.7}\ \mathrm{Myr} \qquad (9)$$

where ζ corresponds to the metallicity in solar units, N_* to the number of SN explosions, E_{51} to the energy per SN in units of 10^{51} erg, and n_0 to the ambient density of the ISM. If we use the parameters evaluated for Ho I in Sect. 4.3 and Sect. 4.4.1 ($N_* = 120$, $n_0 = 0.1\,\mathrm{cm}^{-3}$), assume an energy of 10^{51} erg per SN and the Miller & Hodge (1996) metallicity of 8% solar, we estimate the cooling time $t_{cool} = 3.7\,\mathrm{Gyr}$. This is far too long to play any role in the case of the central shell in Ho I.

If the radius of a shell reaches the 1σ scaleheight of a Gaussian shaped halo, the shock will be accelerated perpendicular to the disk, and metal–enriched material will be ultimately lost to intergalactic space (Silich & Tenorio–Tagle 2001). In this model, neither the pressure of the intergalactic medium nor the gravity of the host galaxy is able to retain the swept–up gas. This is exactly the "blow–out" scenario which was alluded in Sect. 1.

For radii smaller than the scaleheight h, Gaussian stratification leads to models quite similar to the ones with uniform density. At $R = h$ the density is 0.68 times the density in the midplane. As the radial evolution depends on the density as $n^{-1/5}$ (cf. Eq. 7), the radii and velocities in the z direction before break–out will be only slightly larger then the ones derived by the Sedov model in Sect. 4.4.2. However, if one assumes an exponentially–shaped z distribution of the gaseous component, the acceleration and therefore blow–out does not happen until a couple of exponential scalelengths h_{exp} (Silich & Tenorio–Tagle 1998, 2001), which is at about 2.4 times the Gaussian scaleheight h. In this case, one would expect the shell to be still in the Sedov expansion phase with some piled–up gas in the z–direction. However, the latter is not supported by the observational facts.

If blow–out indeed has taken place, it is difficult to estimate how much material was actually lost. The ring seems to dominate the galaxy up to a radius of $125''$ ($\approx 2.1\,\mathrm{kpc}$; see Fig. 6). What may the H I distribution of Ho I have looked like just before the creation of the supergiant shell? We fit different H I profiles to the outer, apparently undisturbed region of the galaxy and extrapolated them back towards the center. This was done for a Gaussian, a linear and an exponential H I distribution (see Fig. 19). If we integrate these profiles, we find that the H I mass corresponding to the Gaussian fit and the one based on our observations are nearly the same, implying that the H I has only been moved around. The linear fit underestimates the observed H I flux by $\sim 30\%$. The exponential profile predicts that $\sim 50\%$ of the H I was lost during the creation of the supergiant shell. Although we have no knowledge

of the nature of the H I distribution of Ho I before the creation of the hole, according to Taylor et al. (1994), many dIrrs show an exponential H I distribution. A further advantage in adopting such a distribution is that this profile exceeds the SF threshold in the inner parts of Ho I out to a radius of ~ 1 kpc, which might explain why the burst of SF was able to occur offset from the dynamical center, as observed.

EDITOR: PLACE FIGURE 19 HERE.

5. SUMMARY

We present high–resolution VLA H I and deep optical UBV(RI)$_c$ as well as Hα observations of the dIrr galaxy Ho I, a member of the M 81 group of galaxies. We find the following:

1. Maps of neutral hydrogen show an impressive supergiant shell with a diameter of 1.7 kpc. In addition, a wealth of small–scale structure is seen in the H I data cube. The shell covers about half of the H I extent of Ho I (total H I size: ~ 5.8 kpc) and contains a substantial fraction ($\sim$75%) of its total neutral gas content (total H I mass: $1.1 \times 10^8\,\mathcal{M}_\odot$). We derive the scaleheight of the H I layer to be $250\,\mathrm{pc} \lesssim h \lesssim 550\,\mathrm{pc}$.

2. A dynamical analysis shows that turbulence plays an important role in Ho I. The velocity dispersion in the north–west ($\sim 12\,\mathrm{km\,s^{-1}}$) is significantly higher than the overall value of $\sim 9\,\mathrm{km\,s^{-1}}$. A tilted ring analysis shows that the dynamical center is offset by 0.75 kpc from the H I morphological center. With the help of a small shell, which has not broken out of the disk yet, we estimate an upper limit of the dark matter content of $\lesssim 3.1 \times 10^8\,\mathcal{M}_\odot$. This leads to a total mass of $\lesssim 5.5 \times 10^8\,\mathcal{M}_\odot$ and an inclination of $10^\circ \lesssim i \lesssim 14^\circ$.

3. Extrapolating backwards in time what the original H I distribution might have looked like before the ring was formed, we estimate a higher neutral gas mass than currently observed. Comparing the results with published models requires that the shell has broken out of the disk. Comparing the results with the H I scaleheight and the overall H I morphology leads to further circumstantial evidence for the occurrence of blow–out in Ho I.

4. With $\mu_\mathrm{B}(0) \sim 24.5\,\mathrm{mag/\Box''}$, Ho I belongs to the class of low–surface brightness dwarf galaxies. The optical extent in the R$_c$ band is comparable to the H I size. Most of the stellar light falls within the H I ring. Azimuthally–averaged surface brightness profiles are shallow from the center outwards to a radius of 1.2 kpc (where the H I column density falls below $\sim 10^{21}\,\mathrm{cm^{-2}}$) and steepen beyond that radius. The luminosity profile can be explained by a rather uniform star formation history in the center of Ho I.

5. The blue luminosity of $L_\mathrm{B} = 1.0 \times 10^8 L_{\mathrm{B}_\odot}$ implies an $\mathcal{M}_\mathrm{HI}/L_\mathrm{B}$ ratio of $1.1\,\mathcal{M}_\odot/L_{\mathrm{B}_\odot}$. We estimate a total visible (stars plus atomic gas) mass of $2.4 \times 10^8\,\mathcal{M}_\odot$.

6. H II regions are found on the outer rim of the H I shell. This implies that conditions in the swept–up H I shell are suitable for star formation to commence. Some of the H II regions on the rim are centered on a smaller H I shell.

7. At the distance of Ho I, bright unresolved optical sources can be either stellar clusters or single stars. A comparison with LMC clusters shows that the cluster population near Ho I is much less abundant (a factor of $\lesssim 1/5$) than that of the LMC. From a comparison with isochrones in the (V, U−B) CMD we find that stars within the H I ring are relatively young ($\sim$15–30 Myr). Not surprisingly, the youngest stars are found to be close to the H II regions on the rim of the H I shell.

8. The age of the stars within the H I shell as well as considerations on the evolution of the gaseous rim lead to an age of the shell of $\sim 80 \pm 20$ Myr. The kinetic energy to create the supergiant shell is some $1.2 \times 10^{53}\,\mathrm{erg} \lesssim E \lesssim 2.6 \times 10^{53}\,\mathrm{erg}$ (equivalent to 120–260 type II SN explosions).

9. The south–eastern side of Ho I is closest to the M 81 triplet and shows a steep gradient in the H I distribution. The opposite side (north–west) shows systematically higher velocity dispersions. Hα emission is predominantly found in the south–east. All of these features may be indicative of ram pressure within the M 81 group. Alternatively, tidal forces might be shaping the structure of the ISM in Ho I at large galactocentric radii.

Ho I is a fascinating object with an impressive supergiant H I shell. Amongst dIrrs with a similar morphology, it is one of the very few nearby, low–mass systems which can be studied in great detail. From our observations it seems likely that the giant H I shell was created by recent star formation within the shell (t$\sim 80 \pm 20$ Myr). We can only speculate what Ho I will look like in, say, 100 Myr and what it looked like before the creation of the H I shell. It may well be that Ho I was a blue compact dwarf galaxy (BCD) in the recent past, with a centrally peaked H I distribution. The active episode of star formation and subsequent SN explosions may have blown the supergiant H I shell that we witness today. In the future the shell may recollapse and, in the process, ignite another burst of massive star formation ("episodic star formation"). In any case, in–depth studies of low–mass and low–metallicity galaxies, such as Ho I, help us understand how the effects of massive star formation change the properties of the interstellar medium. They also give us some insight in to how low–mass galaxies may have contributed to the chemical enrichment of the intergalactic medium when the universe was young.

JO would like to thank Thomas Fritz, Ulrich Mebold and Axel Weiss for fruitful discussions. Without the funding of the Deutsche Forschungsgemeinschaft and the associated Graduiertenkolleg "Magellanic clouds and other dwarf galaxies" this work would not have been possible. The authors also thank the anonymous referee for valuable comments which have helped to improve the presentation of this paper. FW acknowledges NSF grant AST96–13717. EB acknowledges support by CONACyT (grant No. 27606–E). BD acknowledges the award of a Feodor Lynen grant by the "Alexander von Humboldt–Stiftung". Furthermore, we thank the staff of the Calar Alto observatory for their kind support during the observations. This research has made use of the NASA/IPAC Extragalactic Database (NED), which is maintained by the Jet Propulsion Laboratory, Caltech, under contract with the National Aeronautics and Space Administration (NASA), NASA's Astrophysical Data System Abstract Service (ADS) and NASA's SkyView.

REFERENCES

Allen, R. J., & Shostak, G. S. 1979, A&AS, 35, 163
Aparicio, A., & Gallart, C. 1995, AJ, 110, 2105
Begeman, K. G. 1989, A&A, 223, 47
Bertelli G., Bressan A., Chiosi C., Fagotto F., Nasi E. 1994, A&AS, 106, 275
Bica, E., Clariá, J. J., Dottori, H., Santos, J. F. C. Jr., Piatti, A. E. 1996, ApJS, 102, 57
Briggs, D. 1995, Ph.D. thesis, New Mexico Institute of Mining and Technology
Bremnes, T., Binggeli, B., & Prugniel, P. 1998, A&AS, 129, 313
Brinks, E., & Bajaja, E. 1986, A&A, 169, 14
Brinks, E., & Walter, F. 1998 in Proceedings of the Bonn/Bochum–Graduiertenkolleg Workshop "The Magellanic Clouds and Other Dwarf Galaxies", eds. T. Richtler & J. M. Braun (Aachen: Shaker Verlag), 1
Bureau, M., & Carignan, C. 2001, in "Dwarf Galaxies and their Environment", eds. K. S. de Boer, R.–J. Dettmar, & U. Klein (Shaker Verlag: Aachen), in press (astro–ph/0104117)
Burrows, A. 2000, Nature, 403, 727
Bushouse, H. A. 1987, ApJ, 320, 49
Cardelli, J. A., Clayton, G. C., & Mathis, J. S. 1989, ApJ, 345, 245
Chevalier, R. 1974, ApJ, 188, 501
Clark, B. G. 1980, A&A, 89, 377
de Boer, K. S., Braun, J. M., Vallenari, A., Mebold, U. 1998, A&A, 329, 49
De Blok, W. J. G., & Walter, F. 2000, ApJ, 537, L95
De Young, D. S., & Heckman, T. M. 1994 ApJ, 431, 598
Dickel, J. R., & Rood, H. J. 1978, ApJ, 223, 391
Ehlerová, S., Palouš, J., Theis, C., Hensler, G. 1997, A&A, 328, 121
Elmegreen, B. G. 1994, ApJ, 427, 384
Ferrara, A., & Tolstoy, E. 2000 MNRAS, 313, 291
Franco, J., & Cox, D. P. 1986 PASP, 98, 1076
Freedman, W. L., et al. 1994, ApJ, 427, 628
Freeman, K. C. 1970 ApJ, 160, 811
Gallagher, J. S., & Hunter, D. A. 1984, ARA&A, 22, 37
Gerola, H., & Seiden, P. E. 1978, ApJ, 223, 129
Gilmore G. & Wyse R. F. G. 1991, ApJ, 367, L55
Gooch, R. E., 1995, in ASP Conf. Ser. 77, Astronomical Data Analysis Software and Systems IV, eds. R. A. Shaw, H. E. Payne, & J. J. E. Hayes (San Francisco: ASP), 144
Gunn, J. E., & Gott, J. R., III, 1972, ApJ, 176, 1
Hunter, D. A., & Plummer, J. D. 1996, ApJ, 462, 732
Hunter, D. A., Elmegreen, B. G., & Baker, A. L. 1998, ApJ, 493, 595
Hunter, D. A., Elmegreen, B. G., & van Woerden, H. 2001, ApJ, in press (astro–ph/0104091)
Heiles, C. 1979, ApJ, 229, 533
Heiles, C. 1984, ApJS, 55, 585
Hoessel, J. G., & Danielson G. E. 1984, ApJ, 286, 159
Holmberg, E. 1950, Lund. Medd. Astron. Obs. Ser. II, 128,1
Jörsäter, S., & van Moorsel, G. A. 1995, AJ, 110, 2037
Kennicutt, R. C., Jr., Roettiger, K. A., Keel, W. C., van der Hulst, J. M., Hummel, E. 1987, AJ, 93, 1011
Kennicutt, R. C., Jr. 1989, ApJ, 344, 685
Kennicutt, R. C., Jr. 1998, ARA&A, 36, 189
Kim, S., Dopita, M. A., Staveley–Smith, L., & Bessell, M. S. 1999, AJ, 118, 2797
Landolt, A. 1992, AJ, 104, 340
Lang, K. R. 1992, Astrophysical Data: Planets and Stars. (Heidelberg: Springer)
Leitherer, C., et al. ApJS, 123, 3
Lo, K. Y., Sargent, W. L. W., & Young, K. 1993, AJ, 106, 507
Luks, T., & Rohlfs, K. 1992, A&A, 263, 41
Mac Low, M.–M., & McCray, R. 1988, ApJ, 324, 776
Mac Low, M.–M., & Ferrara, A. 1999, ApJ, 513, 142
Makarova, L. 1999, A&AS, 139, 491
McCray, R., & Kafatos, M. 1987, ApJ, 317, 190
Miller, B. W., & Hodge, P. 1994, ApJ, 427, 656
Miller, B. W., & Hodge, P. 1996, ApJ, 458, 467
Mueller, M. W., & Arnett, W. D. 1976, ApJ, 210, 670
Puche, D., Westpfahl, D., Brinks, E., Roy, J.–R. 1992, AJ, 103, 1841
Puche, D., & Westpfahl, D. 1993, in ESO Conf. Workshop Proc. 49, in ESO/OHP Workshop on Dwarf Galaxies, eds. G. Meylan & P. Prugniel (Garching: ESO), 273
Rhode, K. L., Salzer, J. J., Westpfahl, D. J., Radice, L. A. 1999, AJ, 118, 323
Sandage, A., & Tammann, G. A. 1974, ApJ, 191, 603
Sault, R. J., Teuben, P. J., & Wright, M. C. H. 1995, in Astronomical Data Analysis Software and Systems IV, eds. R. Shaw, H. E. Payne, & J. J. E. Hayes, ASP Conf. Ser. 77 (San Francisco: ASP), 433
Schlegel, D. J., Finkbeiner, D. P., & Davis, M. 1998, ApJ, 500, 525
Sedov, L. 1959, Similarity and Dimensional Methods in Mechanics (New York: Academic Press)
Silich, S. A., & Tenorio–Tagle, G. 1998, MNRAS, 299, 249
Silich, S. A., & Tenorio–Tagle, G. 2001, ApJ, 552, 91
Skillman, E. D. 1987, in NASA Conf. Pub. CP–2466, Star Formation in Galaxies, ed. C. J. Lonsdale Persson (Washington: NASA), 263
Skillman, E. D., Terlevich, R., Teuben, P. J., van Woerden, H. 1988, A&A, 198, 33
Staveley–Smith, L., Sault, R. J., Hatzidimitrou, D., Kesteven, M. J., McConnell, D. 1997, MNRAS, 289, 225
Stetson P. B., Davis, L. E., & Crabtree, D. R. 1990, in ASP Conf. Ser. 8, CCDs in Astronomy, ed. G. H. Jacoby (San Francisco: ASP), 289
Stetson P. B. 1987, PASP, 99, 191
Stewart, S. G., & Walter, F. 2000, AJ, 120, 1794
Stil, J. A., Ph.D. thesis, Univ. of Leiden
Taylor, C., Brinks, E., Pogge, R. W., Skillman, E. D. 1994, AJ, 107, 971
Tenorio–Tagle, G., & Bodenheimer, P. 1988, ARA&A, 26, 145
Tikhonov, N. A., Karachentsev, I. D., Bilkina, B. I., & Sharina, M. E. 1992, A&ApTrans, 1, 269
Tody, D. 1993, in ASP Conf. Ser. 52, Astronomical Data Analysis Software and Systems II, eds. R. J. Hanisch, R. J. V. Brissenden, & J. Barnes, (San Francisco: ASP), 173
Toomre, A. 1964, ApJ, 139 1217
Tully, R. B., Bottinelli, L., Fisher, J. R., Gouguenheim, L., Sancisi, R., van Woerden, H. 1978, A&A, 63, 37
van der Kruit, P. C. 1981, A&A, 99, 298
Van Dyk, S., Puche, D., & Wong, T. 1998, AJ, 116, 2341
van Zee, L., Skillman, E. D., & Salzer, J. J. 1998, AJ, 116, 1186
Walter, F., & Brinks, E. 1999, AJ, 118, 273
Walter, F., & Brinks, E. 2001, AJ, 121, 3026
Westpfahl, D., & Puche, D. 1993, in ESO Conf. Workshop Proc. 49, ESO/OHP Workshop on Dwarf Galaxies, eds. G. Meylan & P. Prugniel (Garching: ESO), 295
Wilcots, E. M., & Miller, B. W. 1998, AJ, 116, 2363
Young, L. M., & Lo, K. Y. 1996, ApJ, 462, 203
Young, L. M., & Lo, K. Y. 1997, ApJ, 490, 710
Yun, M. S., Ho, P. T. P., & Lo, K. Y. 1994, Nature, 372, 530

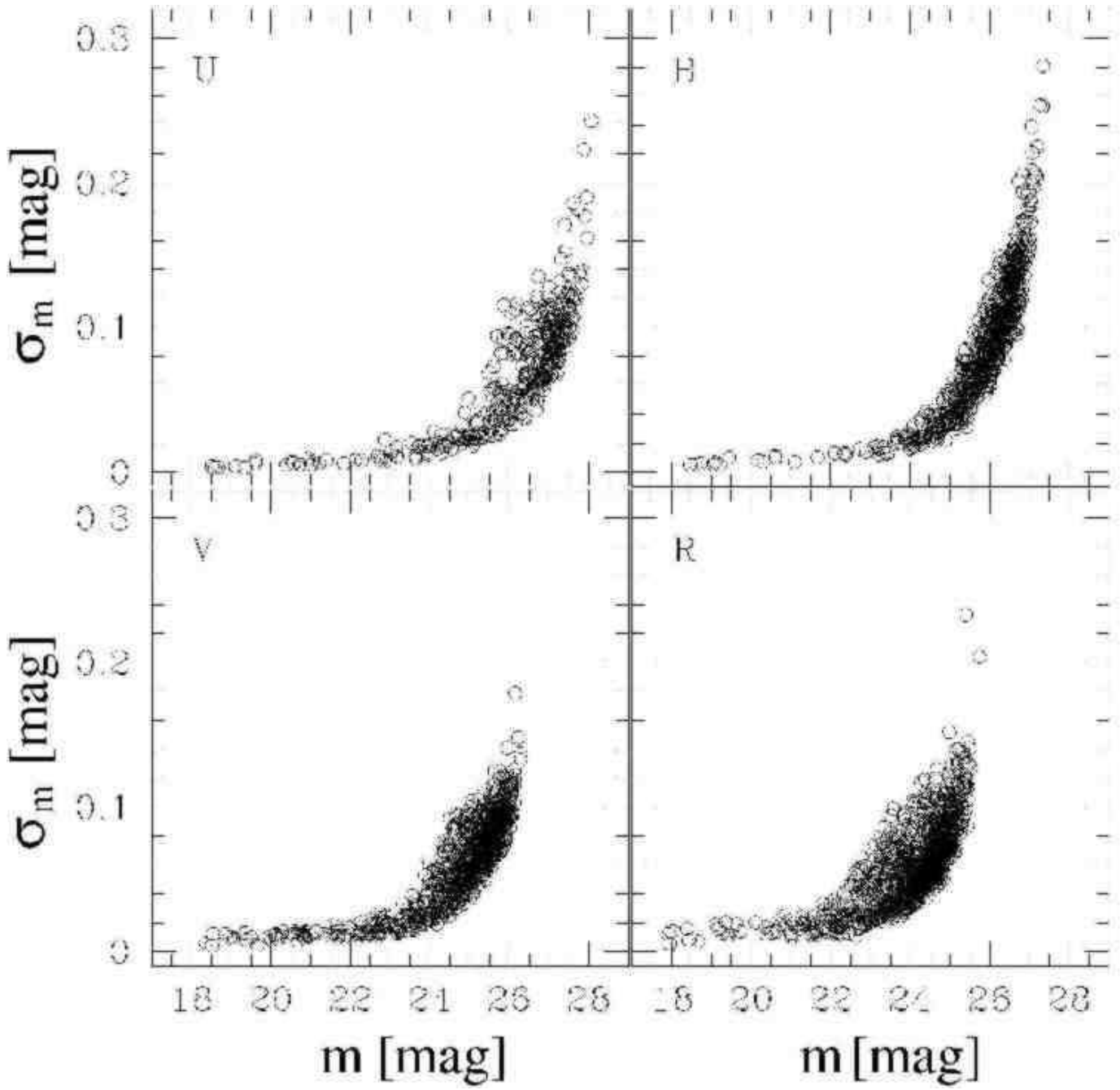

FIG. 1.— Formal photometric errors as a function of magnitude in the UBV(RI)$_c$ bands (output of ALLSTAR in DAOPHOT).

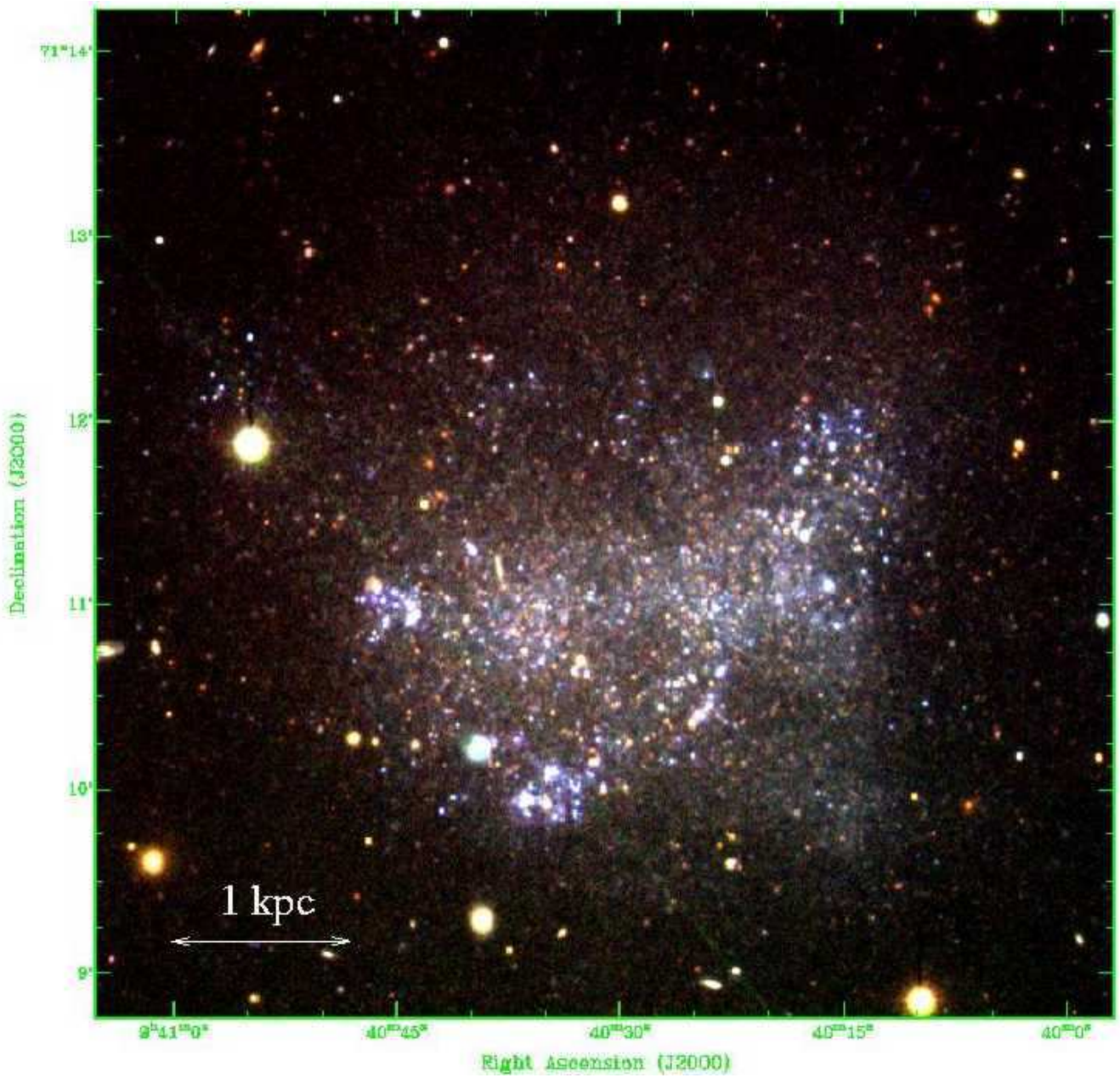

FIG. 2.— Three–color composite image of Ho I based on our UBVR$_c$ CCD frames, where the blue color represents an average image of U and B.

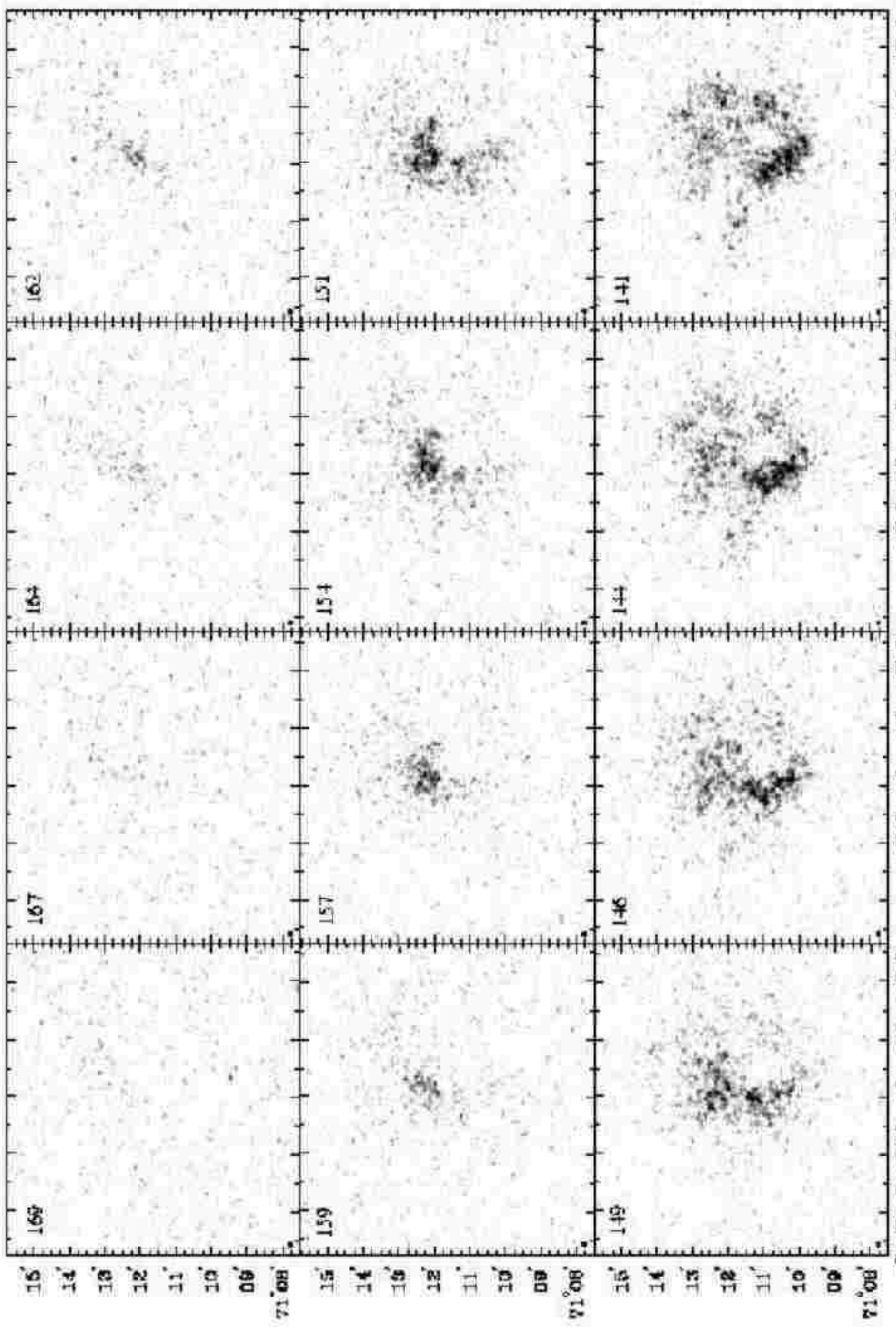
162
151
141
163
154
144
167
157
146
169
159
149
RA (J2000)

FIG. 3.— H I channel maps of Ho I. The shape of the beam is plotted in the lower left, and the (heliocentric) velocity in the upper left corner in units of $\mathrm{km\,s^{-1}}$ ($1'$ corresponds to $\sim$1 kpc). Note the central H I depression in all channel maps and the fact that there is emission in almost every channel map in the north–west. Structures at smaller scales, such as rings or holes, are usually visible in two consecutive maps only.

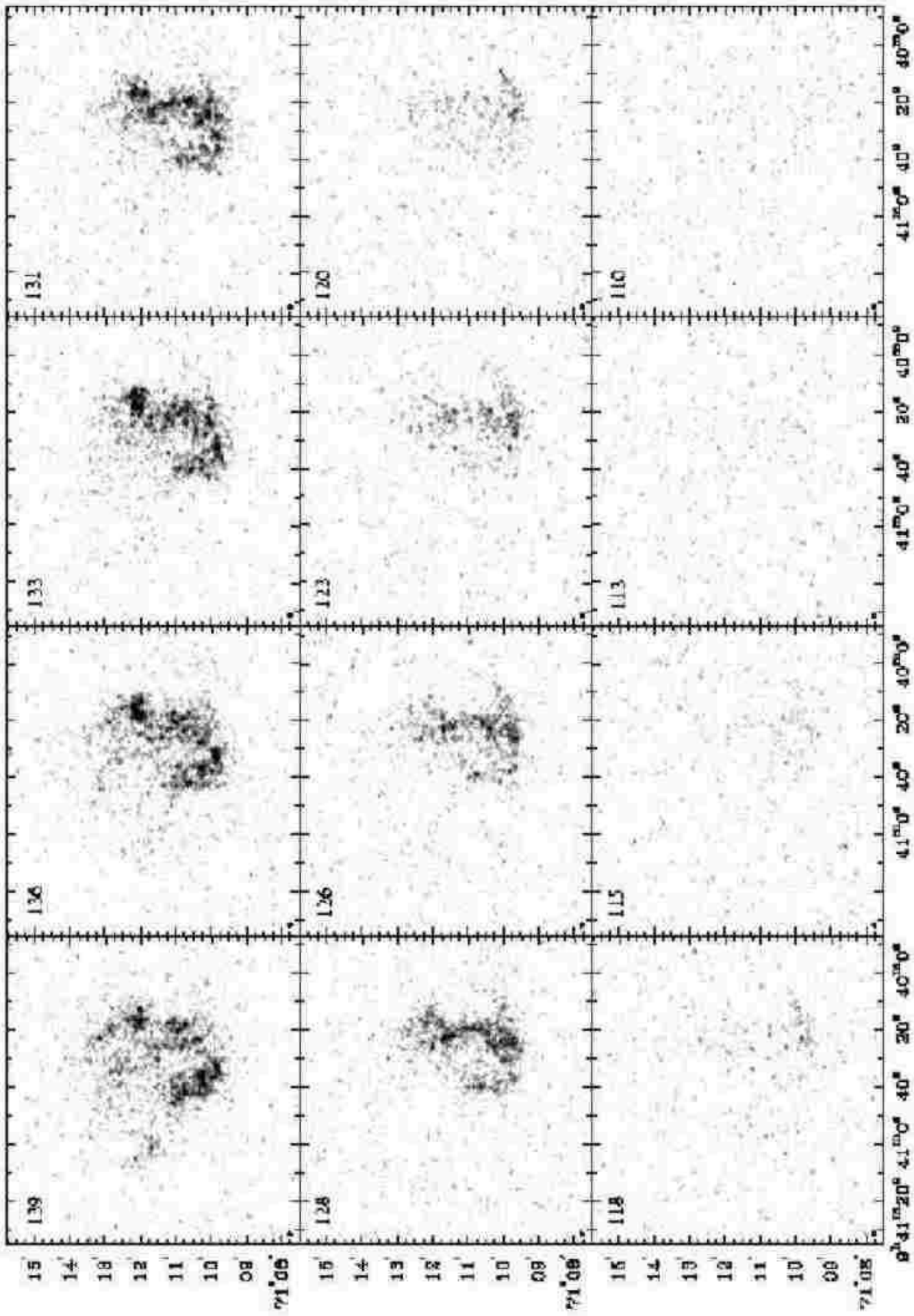
131
120
110
133
123
113
136
126
115
139
128
118
RA (J2000)

FIG. 3.— continued

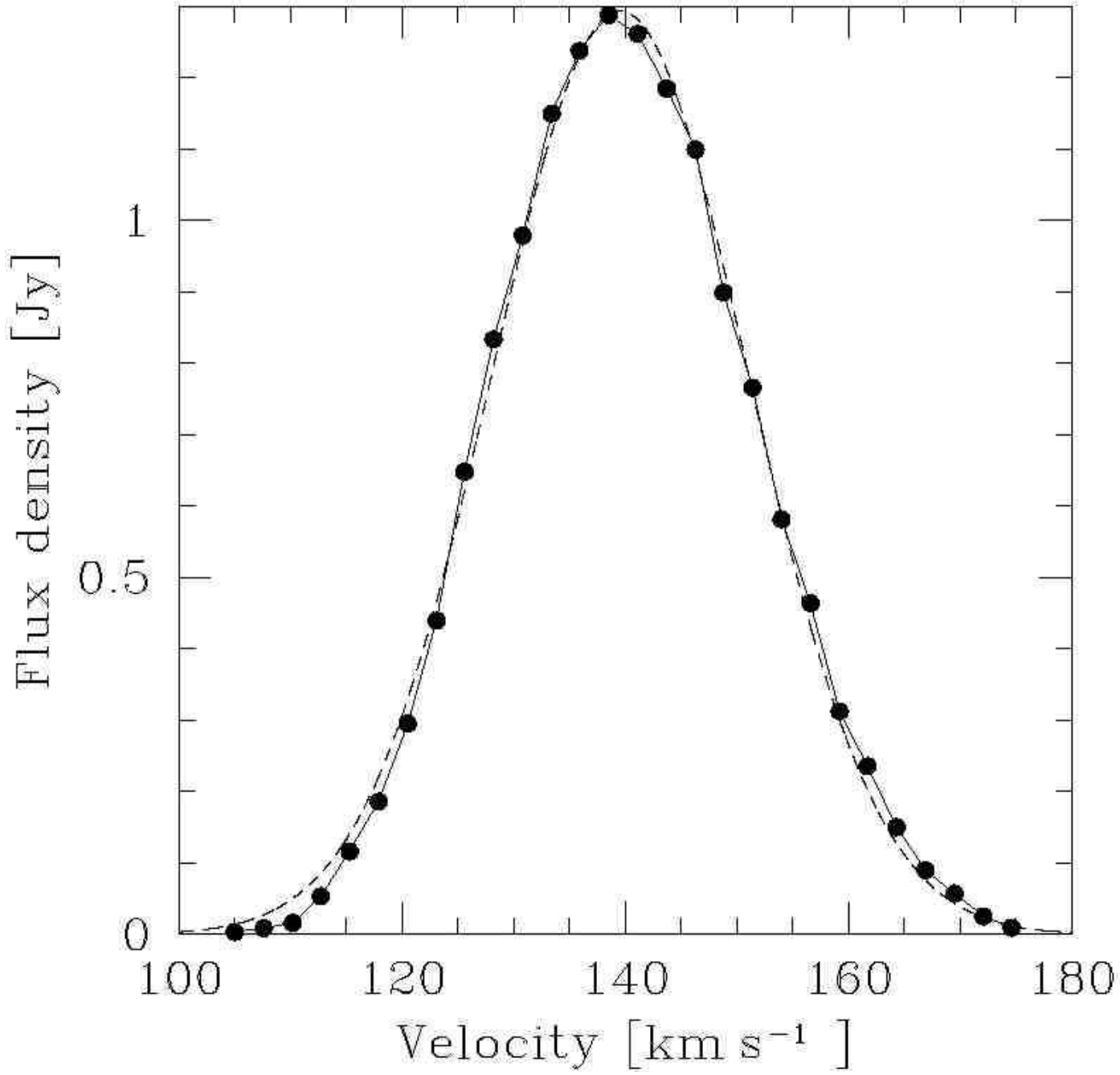

FIG. 4.— H I spectrum of Ho I. The shape is a nearly perfect Gaussian, as illustrated by the *dashed curve*, which is a least–squares fit to the data points. Velocities are heliocentric.

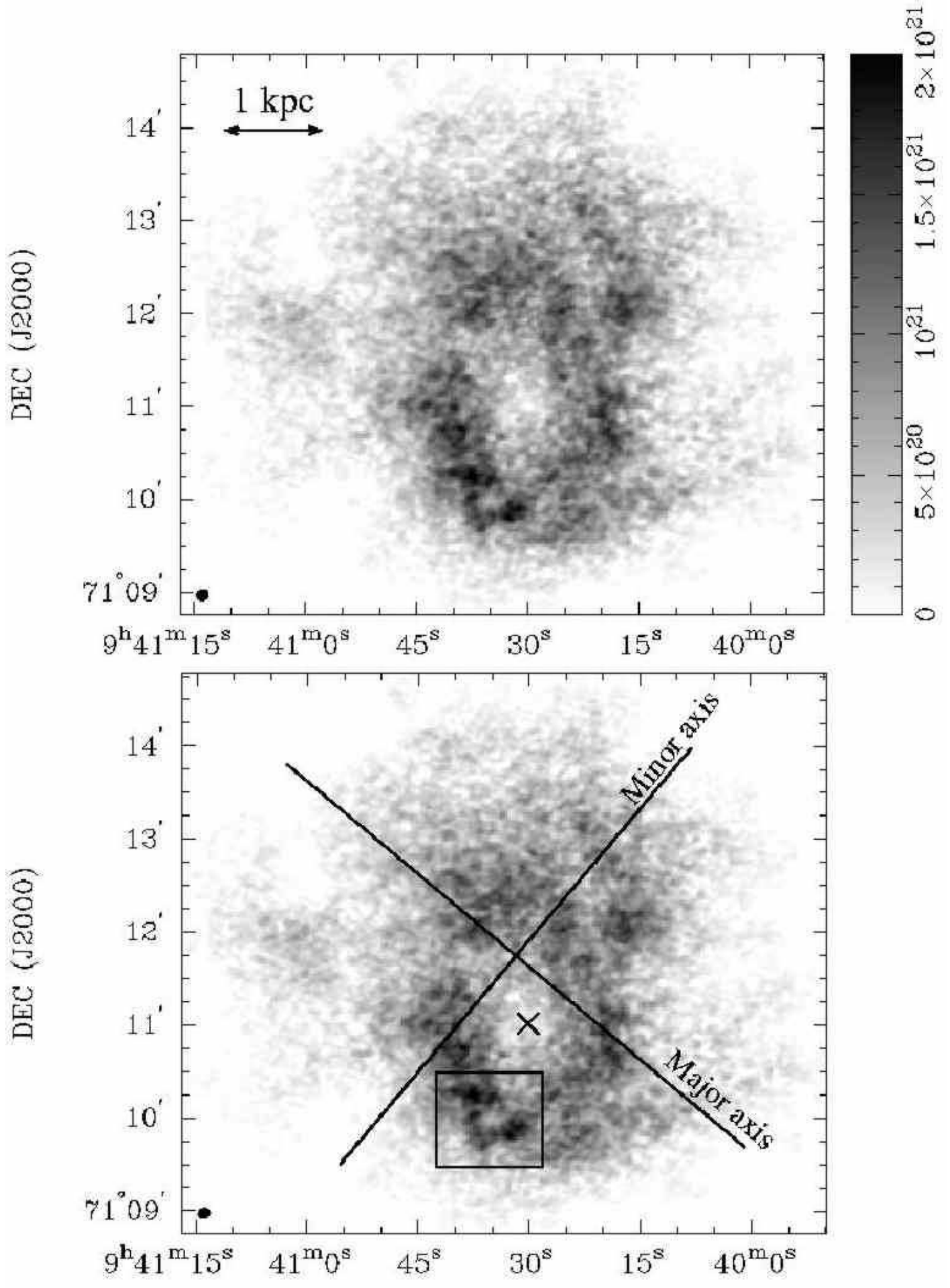
1 kpc
DEC (J2000)
14′
13′
12′
11′
10′
71°09′
9h41m15s
41m0s
45s
30s
15s
40m0s
0
5×10^20
10^21
1.5×10^21
2×10^21
Minor axis
Major axis

FIG. 5.— *Upper panel:* The integrated H I emission of Ho I. The beam of $8\farcs2 \times 7\farcs0$ in size is shown in the lower left corner. *Lower panel:* The same figure as above, but with the kinematical major and minor axes overlaid. The cross indicates the morphological center, i.e., the point where the H I density reaches its minimum. The box shows the region discussed in Sect. 4.6. A blow–up of this area is shown in Fig. 18.

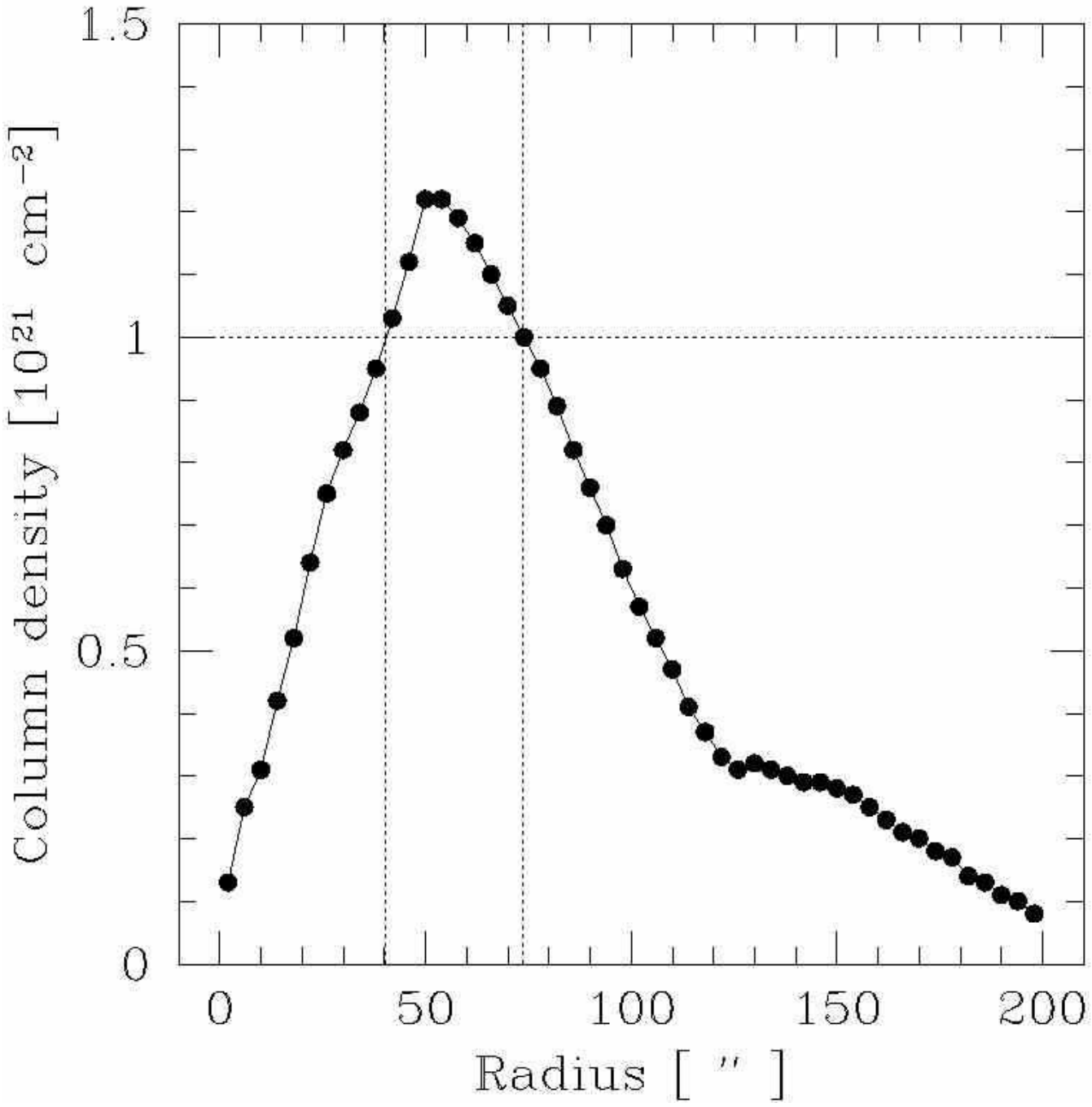

FIG. 6.— Azimuthally–averaged H I distribution, taking the morphological center (cf. Fig. 5) as the origin ($1'$ corresponds to $\sim$1 kpc). The vertical lines represent the radii where the H I column density reaches values sufficiently high for star formation to commence ($N_{\rm HI} = 10^{21}$ cm^{-2}).

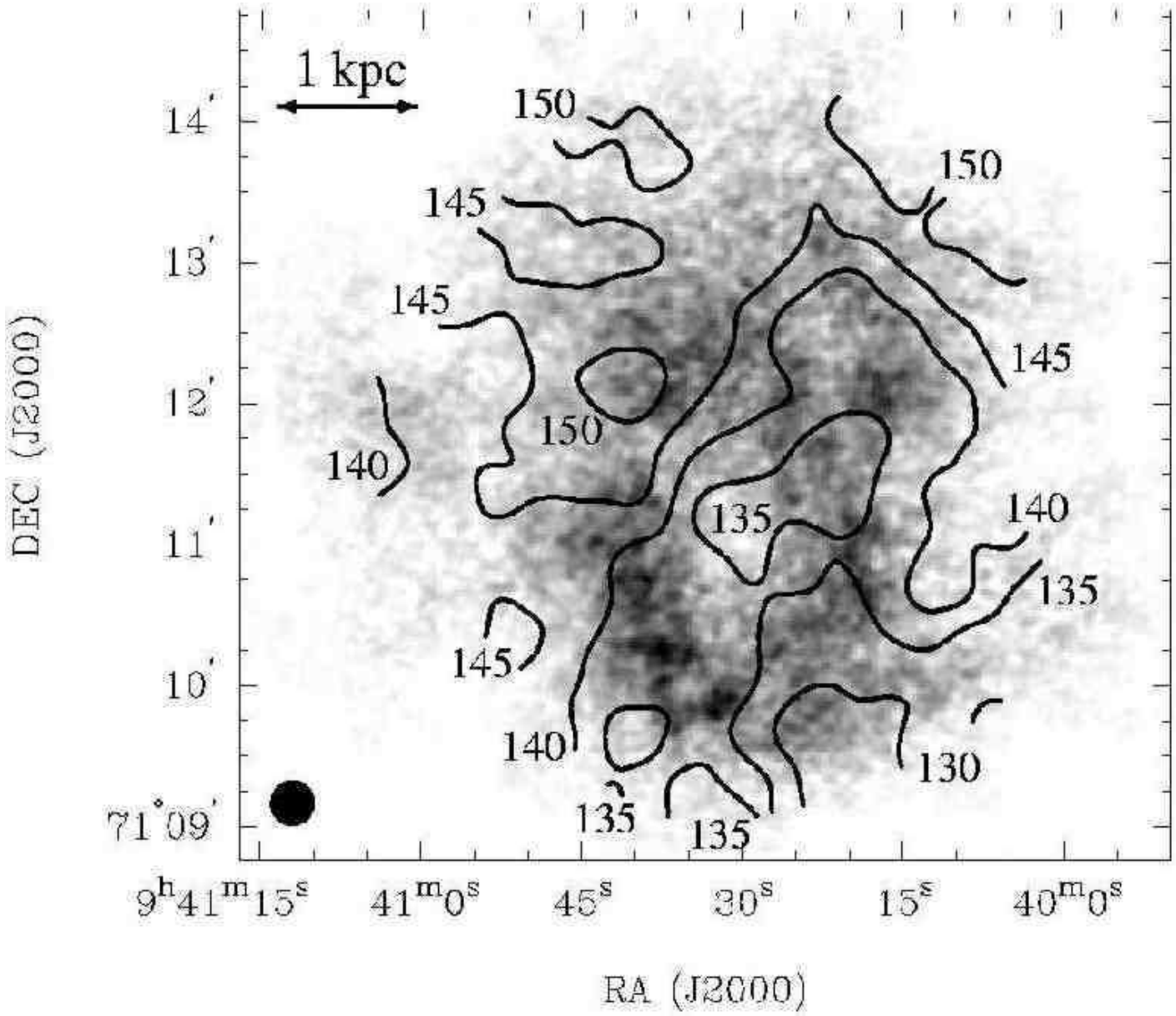

FIG. 7.— Velocity field of the H I data of Ho I, smoothed to 20″, plotted as contours overlaid on a greyscale representation of the integrated H I map (units are km s^{-1}).

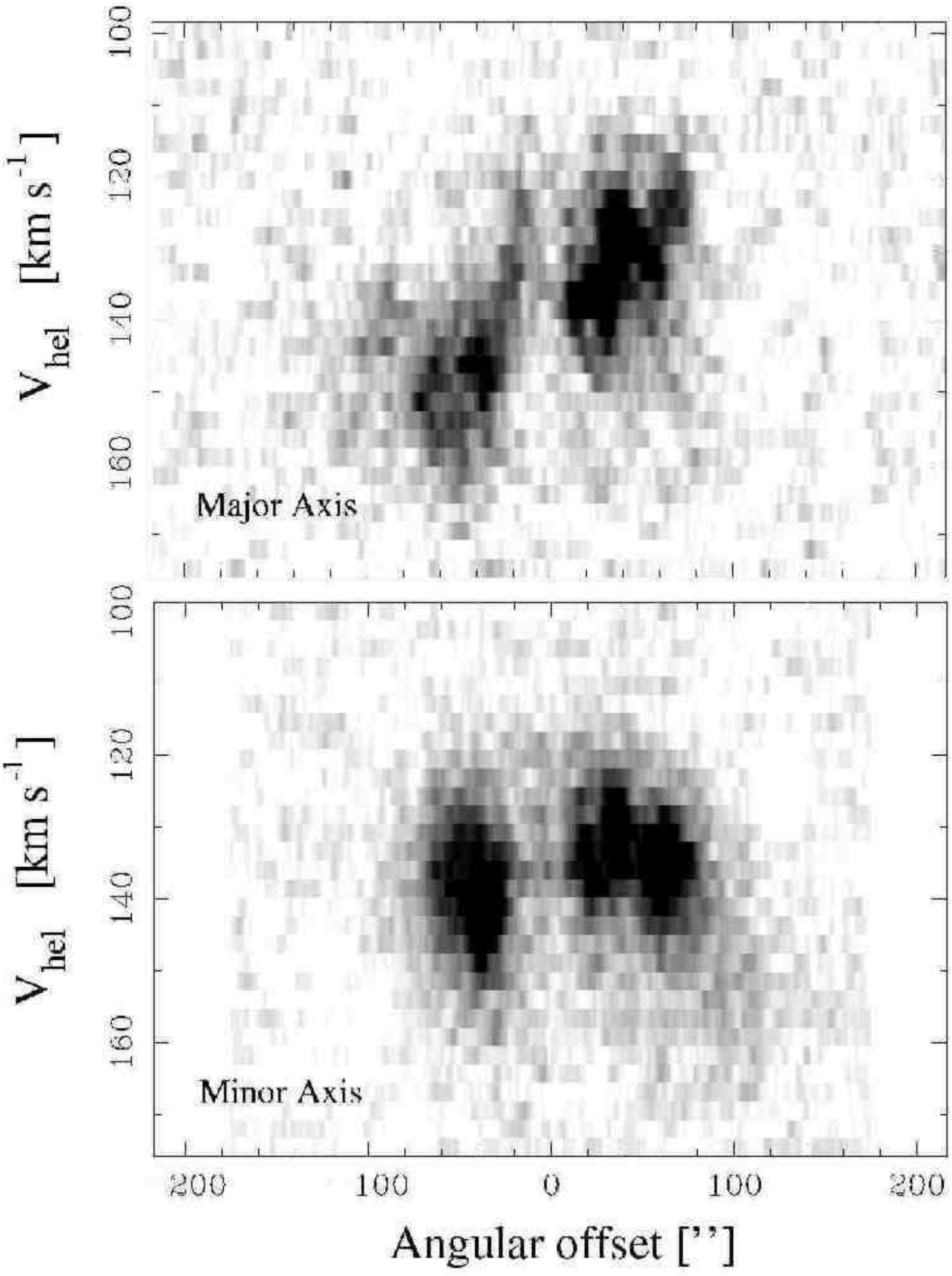
Major Axis
Minor Axis
V hel [km s-1]
V hel [km s-1]
100
120
140
160
200
100
0
100
200
Angular offset ['']

FIG. 8.— Position–velocity cuts parallel to the major and minor axis and centered on the morphological center of lowest H I column density in the hole (cf. Fig. 5). Positive offsets point to the north–west (major axis) and to the south–west (minor axis). $1'$ corresponds to $\sim$1 kpc.

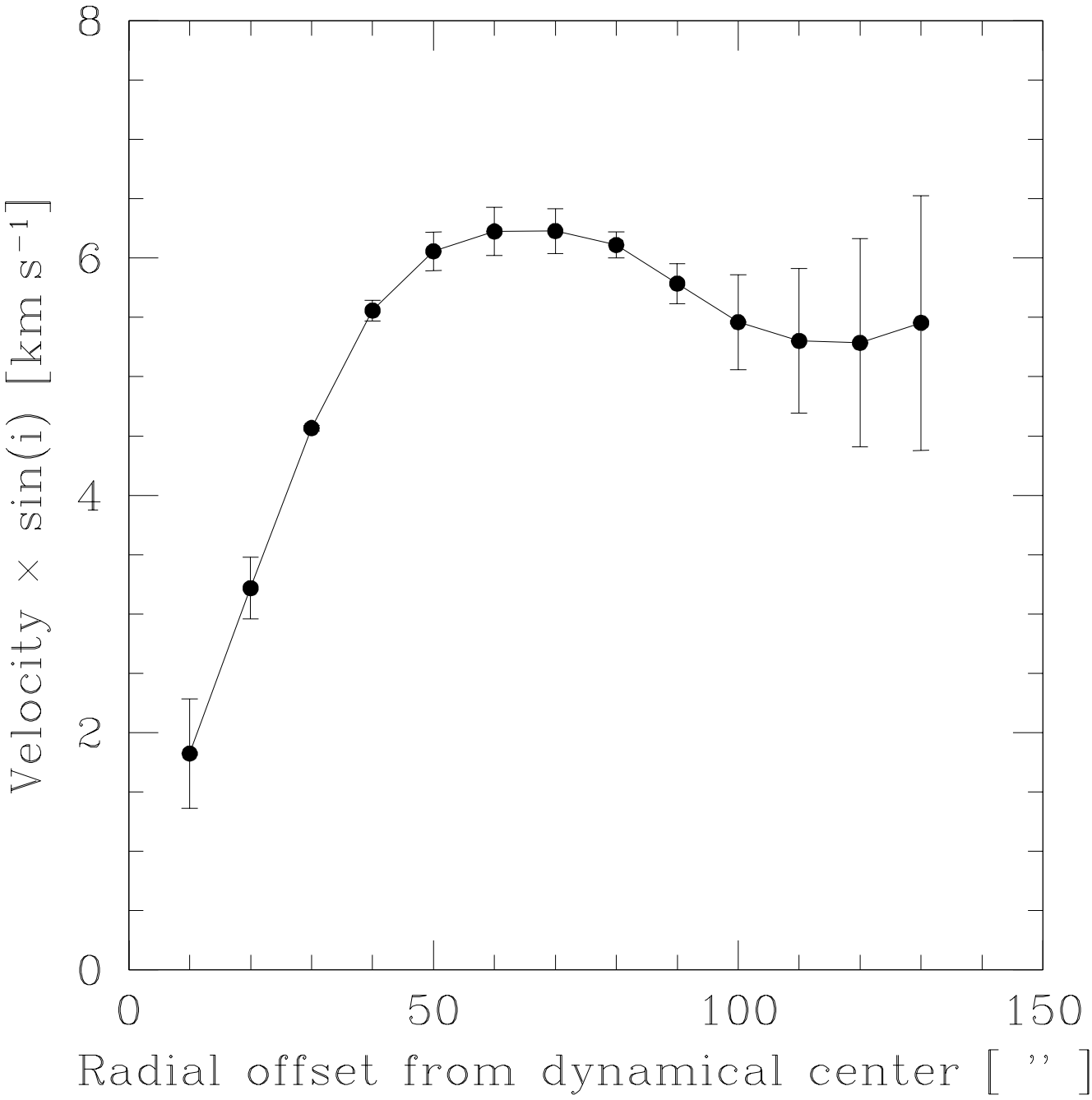

FIG. 9.— Observed rotational velocity ($V \times \sin i$) curve of Ho I. The error bars reflect the difference in rotational velocity between the approaching and receding sides of the galaxy.

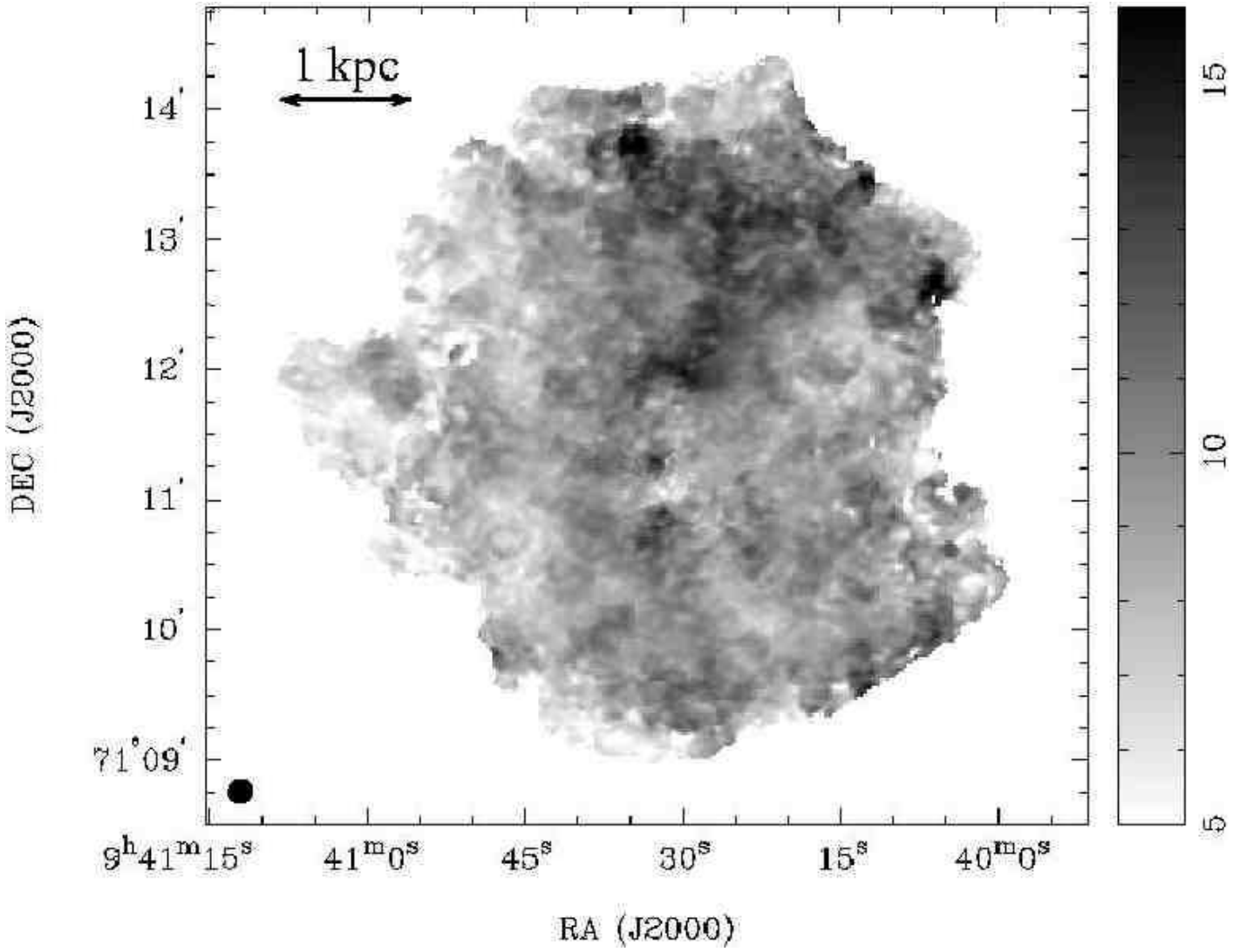

FIG. 10.— H I velocity dispersion of Ho I. In the north–west, the values are systematically higher at $\sim 12\,\mathrm{km\,s^{-1}}$ as compared to the rest of the galaxy ($\sim 9\,\mathrm{km\,s^{-1}}$). This image was derived using the naturally–weighted data which have a resolution of $11\farcs8 \times 11\farcs0$, as indicated in the lower left hand corner.

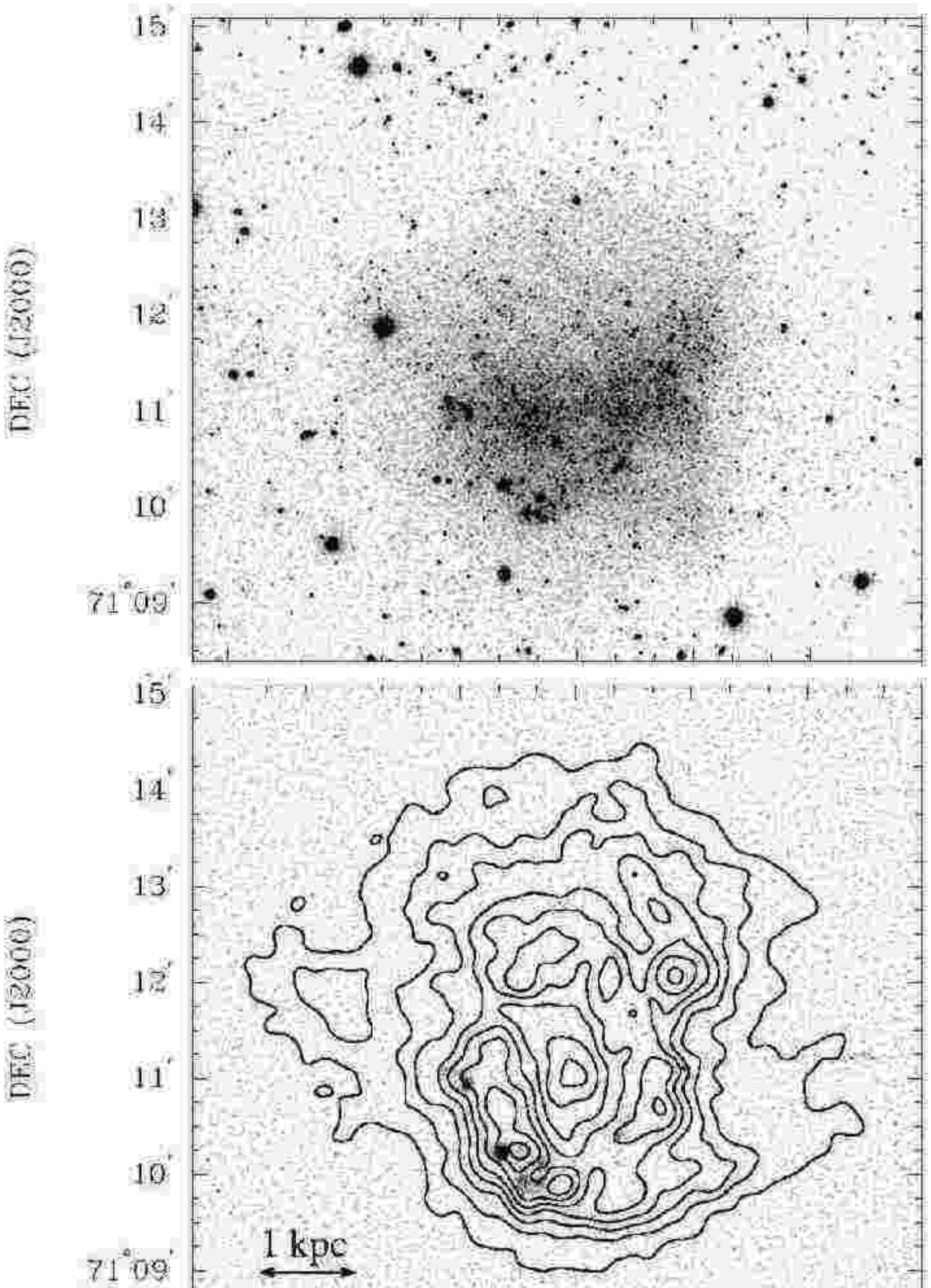
15′
14′
13′
12′
11′
10′
71°09′
DEC (J2000)
15′
14′
13′
12′
11′
10′
71°09′
DEC (J2000)
1 kpc

FIG. 11.— *Upper panel*: Optical R_c band image of Ho I. *Lower panel*: Continuum–subtracted Hα image, at the same scale, with contours of the integrated H I column density smoothed to 15″. Contour levels are drawn at 2×10^{20} cm^{-2} intervals, starting at 1×10^{20} cm^{-2}. The optical radiation is mainly emitted in the southern region of Ho I, within a roughly rectangular area which shows an abundance of bright, mainly blue stars. The extent over which the R_c band emission and the H I distribution are visible are nearly the same.

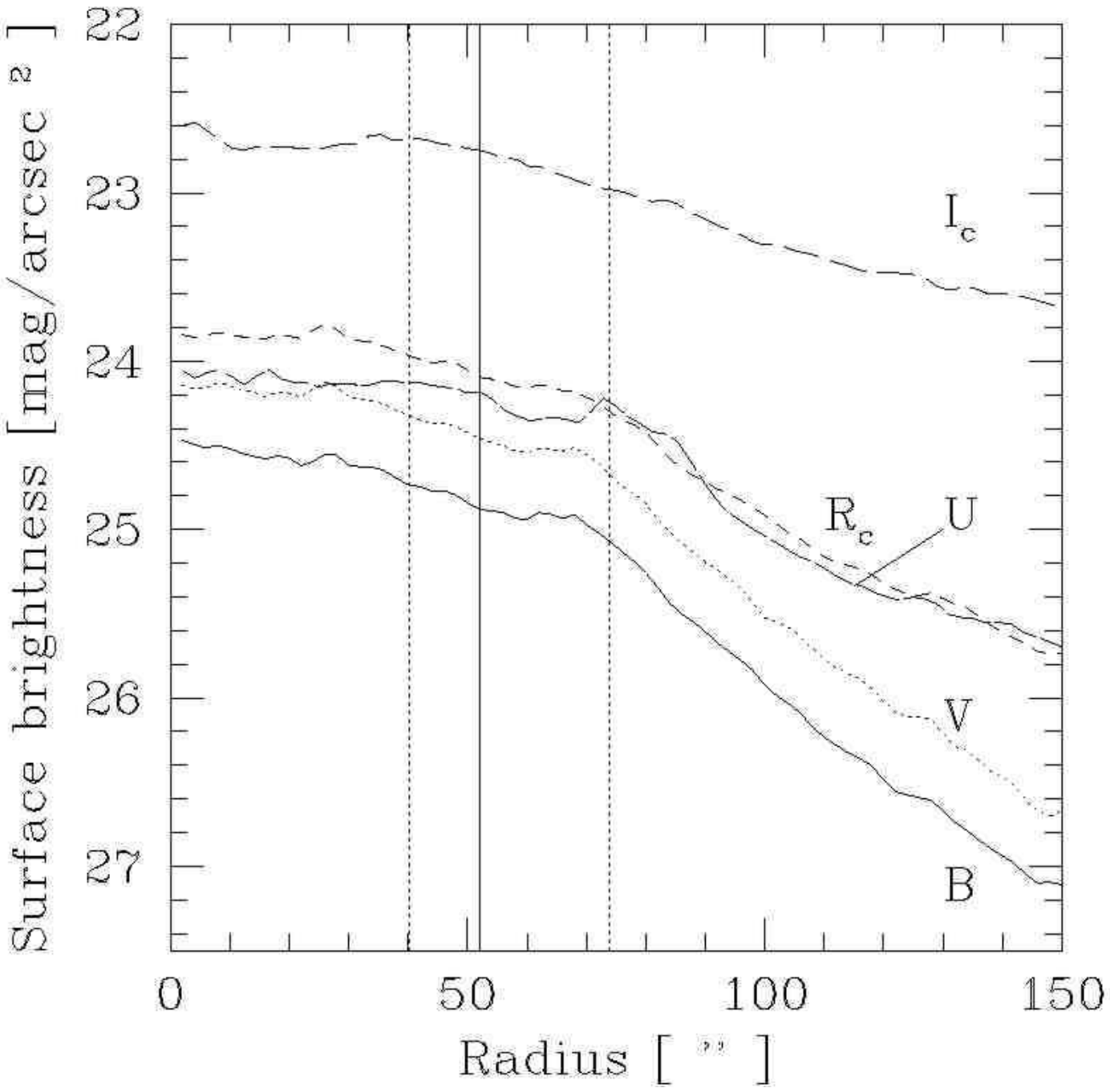

FIG. 12.— Azimuthally–averaged UBV(RI)$_c$ surface brightness distributions with respect to the morphological center of the H I column density distribution (cf. Fig. 6). At a radius of $\sim 70''$ (≈ 1.2 kpc) there is a change in slope, diminishing in importance with increasing wavelength. The vertical lines correspond to the location of the maximum surface density of the H I ring (*solid line*) and the range where the H I column density exceeds the putative star formation threshold, $N_{\rm HI} = 10^{21}$ cm^{-2} (*dotted lines*); see also Figs. 6 and 13.

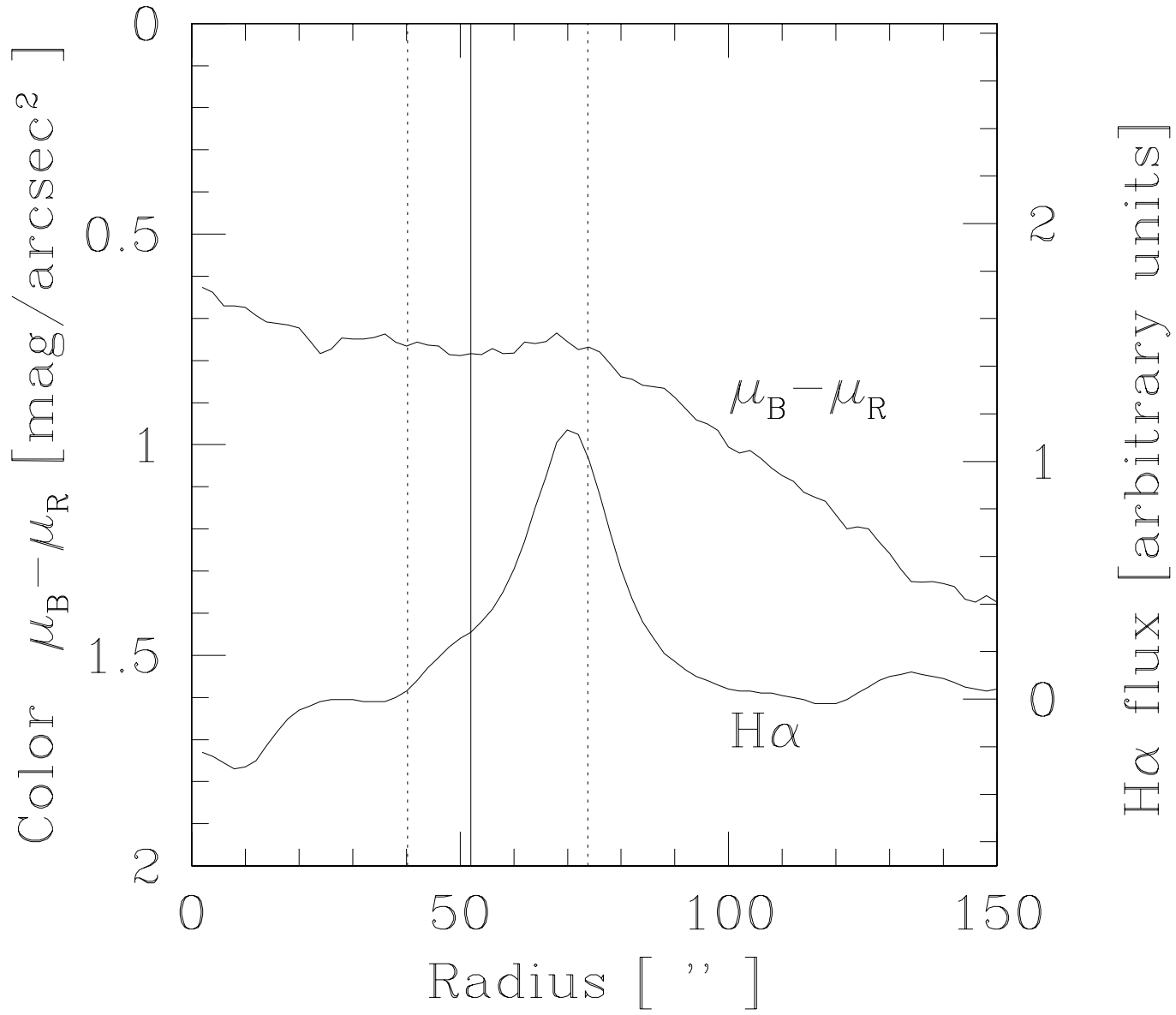

FIG. 13.— Azimuthally–averaged B−R$_c$ color (in mag/□″, *upper graph*) and the smoothed Hα emission as a function of radius in arbitrary units (*lower graph*). Note that the Hα peak and the change in slope in the B−R$_c$ graph are coincident with the change in slope of all colors at a radius of $\sim 70''$ (≈ 1.2 kpc); see also Fig. 12. The *solid vertical line* shows the peak position of the H I ring, whereas the *dotted lines* are drawn at the star formation threshold ($N_{\rm HI} = 10^{21}\,{\rm cm}^{-2}$).

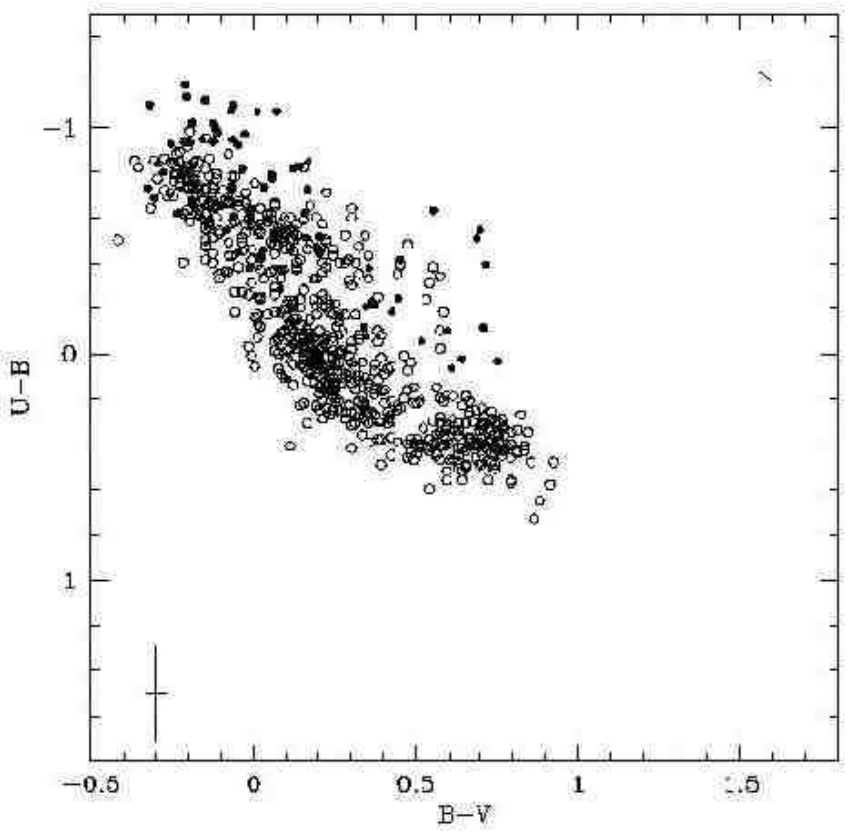
U−B
B−V
−1
0
1
−0.5
0
0.5
1

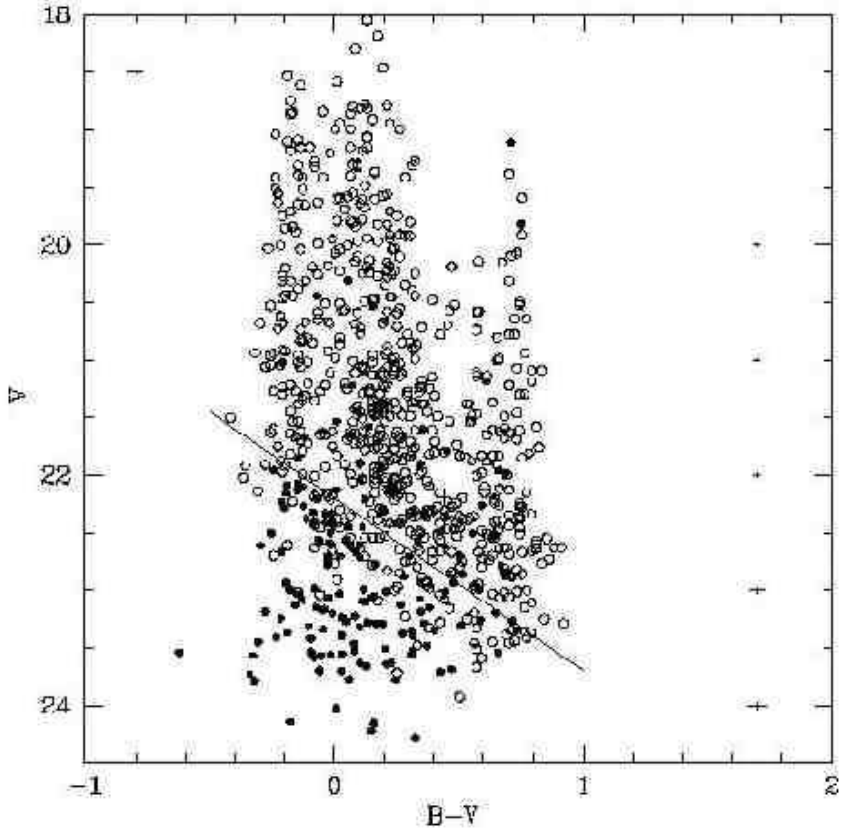
V
B−V
18
20
22
24
−1
0
1
2

FIG. 14.— *Filled circles*: (U−B, B−V) color–color diagram and (V, B−V) color–magnitude diagram of Ho I. *Open circles*: LMC cluster distribution (Bica et al. 1996). A reddening correction corresponding to that towards the position of Ho I has been applied. The calibration error in the color–color diagram is plotted in the lower left. In the same diagram, the reddening vector of Ho I is shown in the upper right. The errors in the CMD are the same as in Fig. 15.

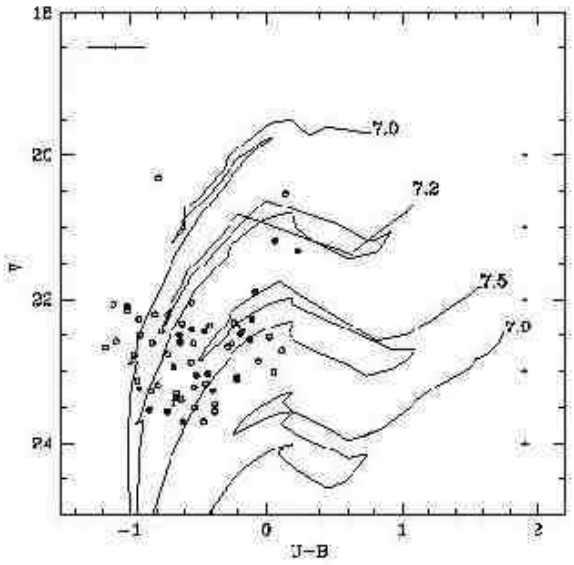
18
20
22
24
V
7.0
7.2
7.5
7.9
−1
0
1
2
J−B

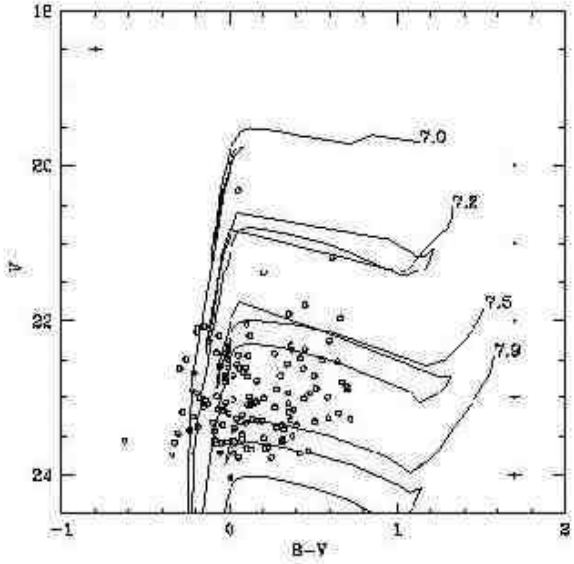
18
20
22
24
V
7.0
7.2
7.5
7.9
−1
0
1
2
B−V

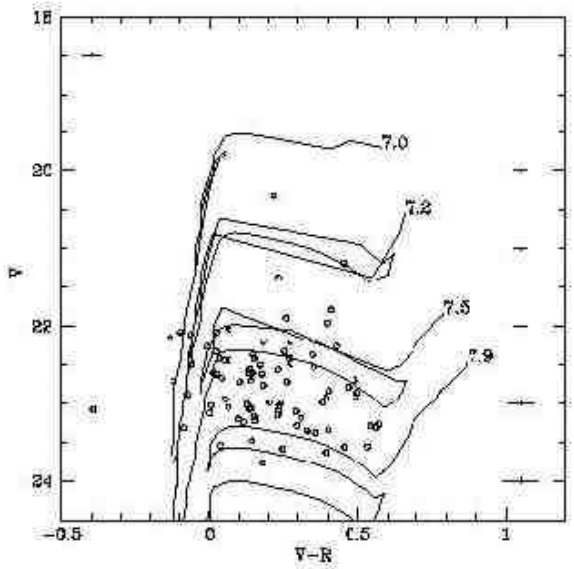
18
20
22
24
V
7.0
7.2
7.5
7.9
−0.5
0
0.5
1
V−R

FIG. 15.— Color–magnitude diagrams of Ho I. The errors on the right side of the panels are the magnitude–dependent formal errors given by the task ALLSTAR. In the upper left corners, the photometric calibration errors are shown. Isochrones from Bertelli et al. (1994) for a metallicity of Z=0.001 are overplotted with the logarithmic age in years. These isochrones are reddened according to the Galactic foreground values at the position of Ho I. The *filled circles* in the (V, U−B) diagram are all the stars within a radius of 0.′9, *inside* the H I ring.

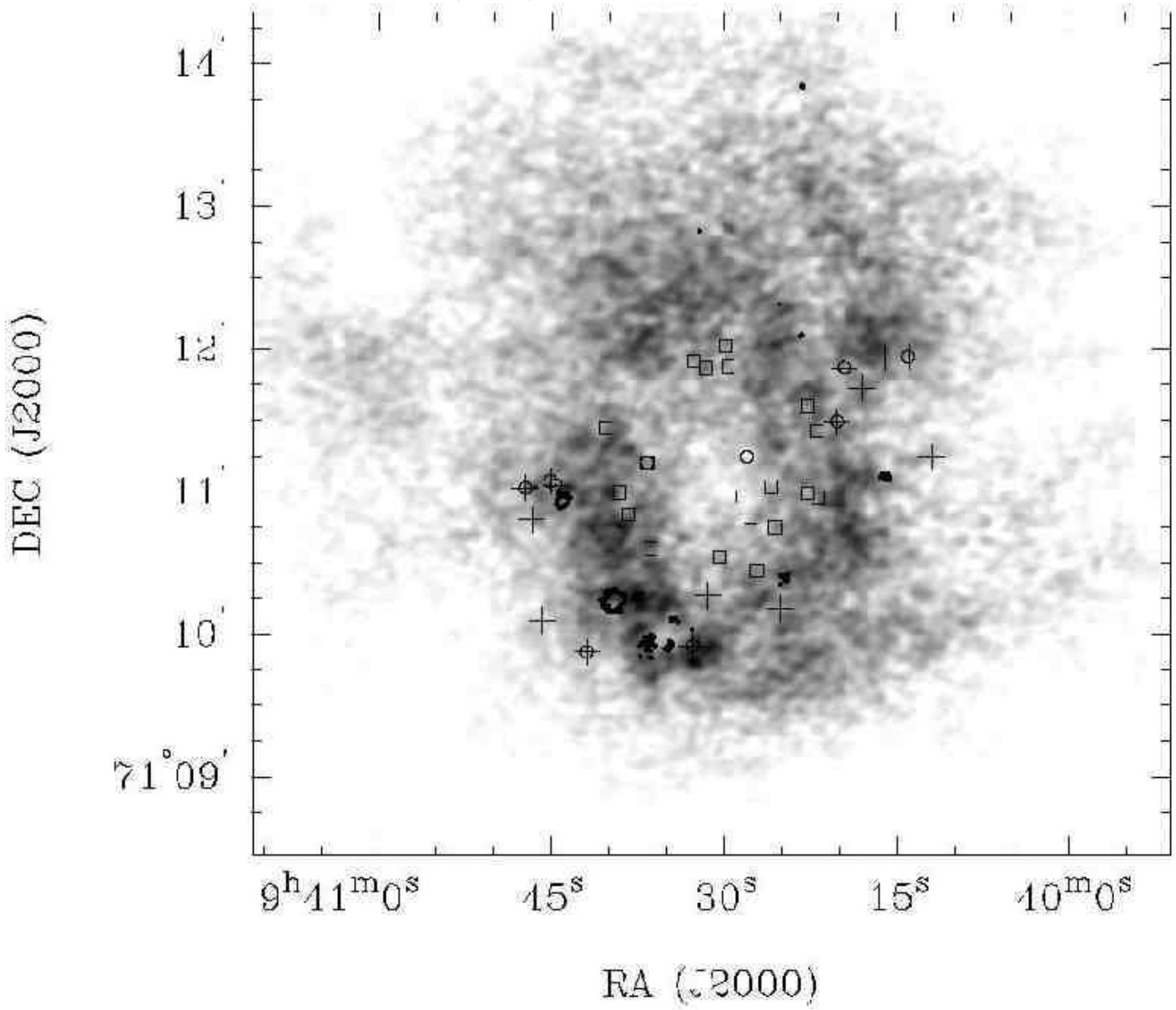

FIG. 16.— Integrated H I of Ho I with Hα emission as contours. The markers show the location of young stars selected on the basis of the (V, U−B) diagram under the condition (U−B)$\lesssim -0.7$ and V$\lesssim$ 23 (*crosses*). The *circles* are stars taken from the (V, B−V) diagram with (B−V)$\lesssim -0.1$ and V$\lesssim$ 23. The *open squares* show the location of the stars plotted in Fig. 15 as *filled circles*.

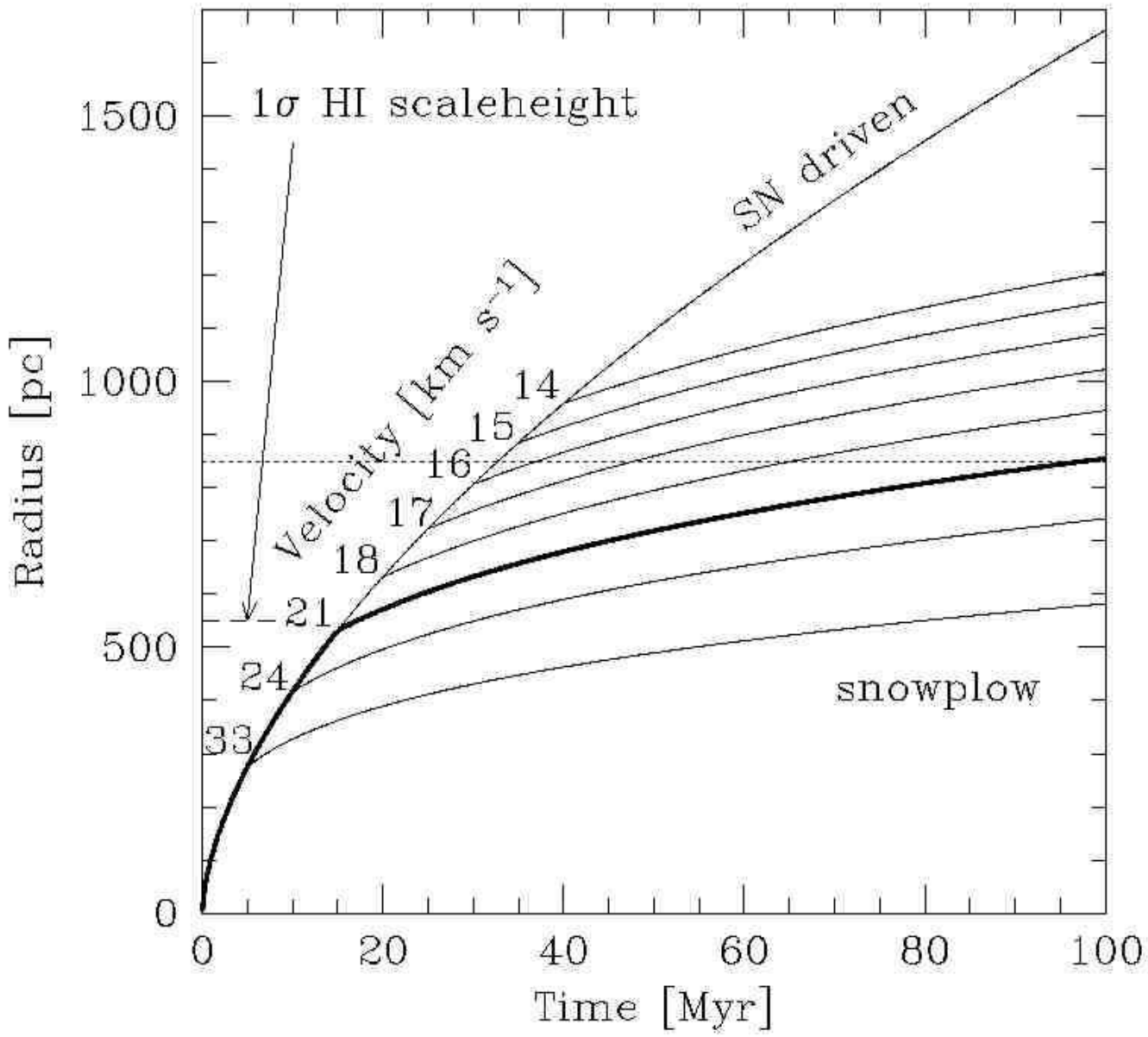

FIG. 17.— Evolution of the supergiant H I shell which dominates Ho I according to the models discussed in the text (Sect. 4.4). After a certain period of SN–driven expansion the shell enters the "snowplow" phase, due to break–out or cooling. The turn–off points are plotted for critical times t_c=5–40 Myr in steps of 5 Myr. The *dotted line* indicates the observed present–day radius of the supergiant shell. The *dashed line* represents the 1σ scaleheight of the H I layer of Ho I. Expansion velocities, derivatives of the radial evolution, are given at the time of the break–out.

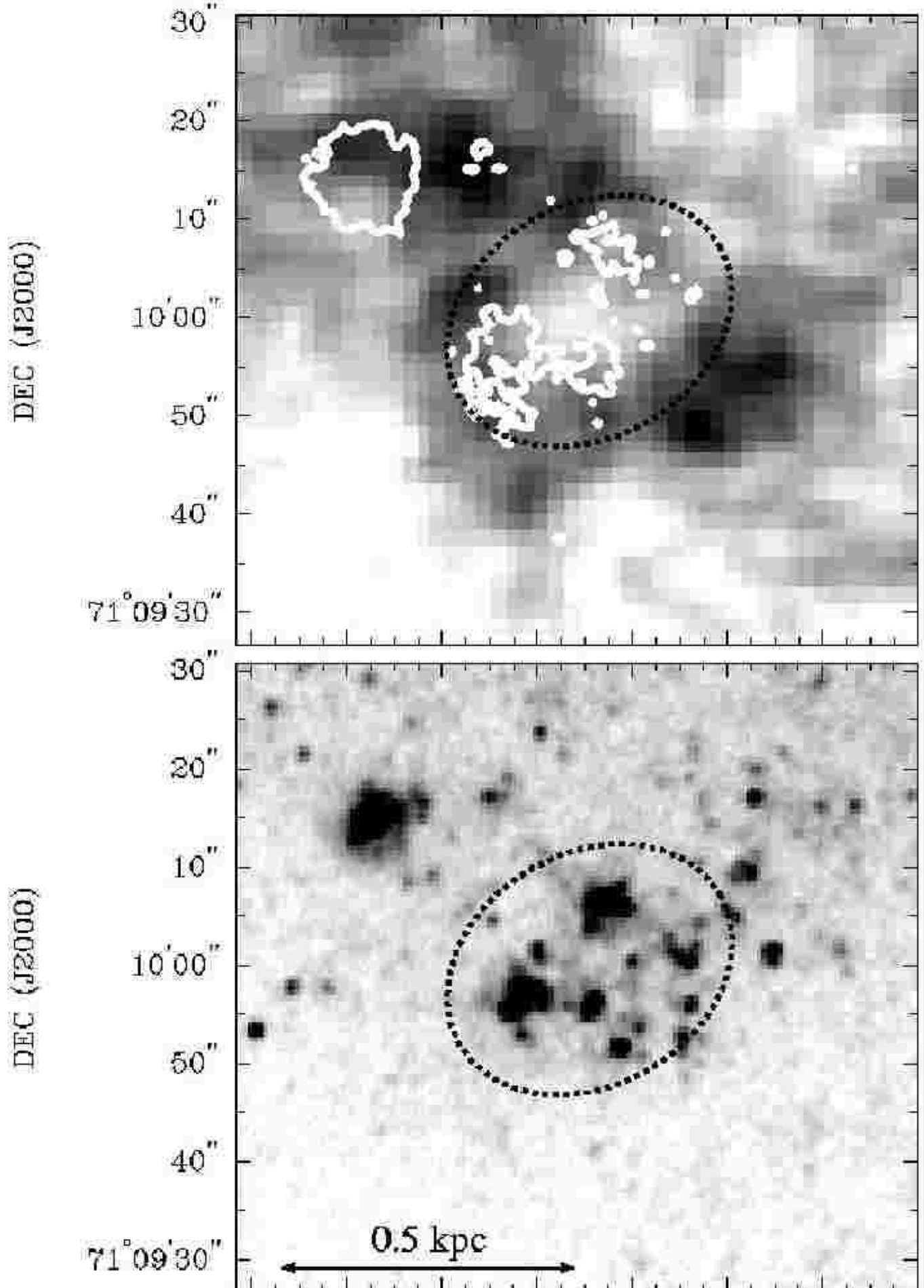
30"
20"
10"
10'00"
50"
40"
71°09'30"
DEC (J2000)
30"
20"
10"
10'00"
50"
40"
71°09'30"
DEC (J2000)
0.5 kpc

FIG. 18.— Blow–up of the box marked in Fig. 5. *Upper panel*: Hα emission overlaid as white contours on the H I content. *Lower panel*: Johnson B image. Both images are at the same scale. The ellipse indicates the size and orientation of the H I shell.

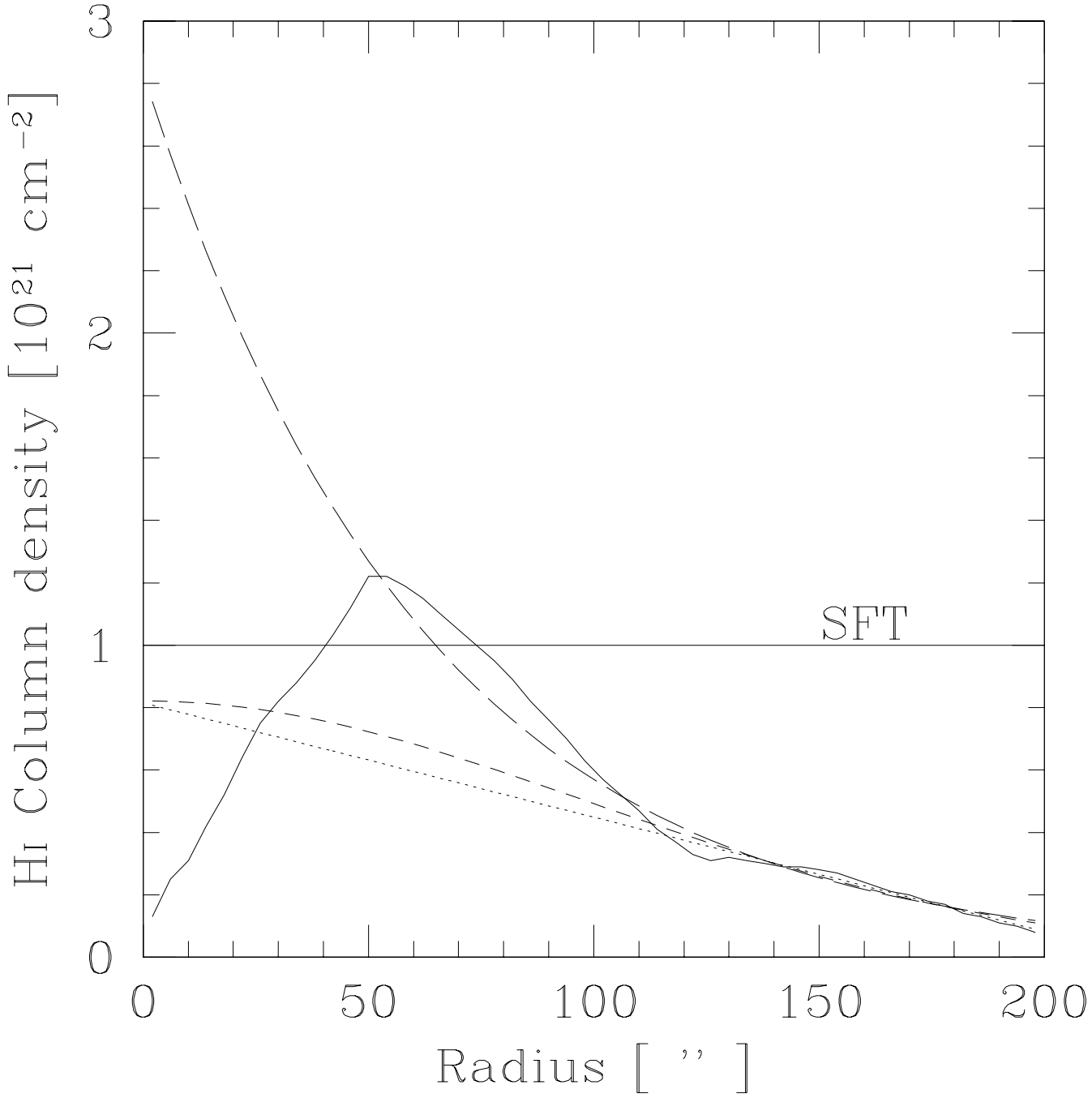

FIG. 19.— Radial H I distribution of Ho I (*solid*) with three different extrapolations towards the center, in an attempt to estimate the amount of H I which might have been present before the energetic events which created the giant hole; exponential (*long dashed*), Gaussian (*short dashed*) and linear (*dotted*) extrapolation. The horizontal line labelled "SFT" displays the empirical SF threshold at $N_{\rm HI} = 10^{21}$ cm^{-2}.

	VLA configuration		
	B	C	D
Date of observation	1990 Jul 23	1990 Dec 02	1991 Mar 07
Time on source	340 min	115 min	97 min
Secondary Calibrator	0917+624	0836+710	0836+710
Coordinates of pointing center (B1950.0)	$\alpha = 09^h\,36^m\,00^s$, $\delta = 71°24'47''$		
Primary Calibrator	3C286		
Number of channels	102		
Velocity range	$321.39 - 58.59\,\mathrm{km\,s^{-1}}$		
Channel width	$2.6\,\mathrm{km\,s^{-1}}$		
Primary Beam (HPBW)	$32'$		
Synthesized Beam (HPBW)			
"natural" weighting	$11\farcs8\times11\farcs0$		
"uniform" weighting	$6\farcs0\times4\farcs7$		
"robust" weighting	$8\farcs2\times7\farcs0$		
1σ rms per channel map ("robust" weighting)	$1.40\,\mathrm{mJy\,beam^{-1}}$		

Table 1
Properties of the VLA H I observations.

Johnson (Cousins) Band	U	B	V	R_c	I_c
Apparent magnitude [mag]	13.23	13.25	12.49	12.40	11.87
Absolute magnitude [mag]	−14.57	−14.55	−15.31	−15.40	−15.93
Mean surface brightness [mag/□″]	25.35	25.37	24.61	24.52	23.99
Central surface brightness [mag/□″]	24.06	24.47	24.15	23.84	22.60
Blue luminosity $[L_{B_\odot}]$	1.0×10^8				
$\mathcal{M}_{HI}/L_B$ $[\mathcal{M}_\odot/L_{B_\odot}]$	1.1				

Table 2
General optical properties of Ho I. The mean surface brightness is based on a circular area with a radius of 150″.

Object Name	Ho I (UGC 5139, DDO 63)
Position (J2000)	$\alpha = 09^h40^m32\overset{s}{.}3, \delta = +71°10'56''$
Morphological type[a]	IAB(s)m
Adopted distance	3.6 Mpc (m−M=27.80 mag)
Scale at this distance	$1' \,\hat{\approx}\, 1$ kpc
H I diameter	5.8 kpc
Systemic velocity	141.5 km s^{-1}
Inclination	$10° \lesssim i \lesssim 14°$
H I linewidth (FWHM)	27.1 km s^{-1}
Total H I flux	36.0 ± 4.0 Jy km s^{-1}
Total H I mass	$1.1{\times}10^8\,\mathcal{M}_\odot$
Mean H I column density	$3.9{\times}10^{20}$ cm^{-2}
Peak H I column density	$2.0{\times}10^{21}$ cm^{-2}
Average midplane H I particle volume density	$0.10\,\mathrm{cm}^{-3} \lesssim n_0 \lesssim 0.20\,\mathrm{cm}^{-3}$
Average H I 1σ scaleheight	$250\,\mathrm{pc} \lesssim h \lesssim 550\,\mathrm{pc}$
Mean H I velocity dispersion	9 km s^{-1}
Total mass	$\lesssim 5.5 \times 10^8\,\mathcal{M}_\odot$
Dark matter content	$\lesssim 3.1 \times 10^8\,\mathcal{M}_\odot$
Dynamical center (J2000)	$\alpha = 09^h40^m31.6^s$, $\delta = 71°11'45''$
Morphological center (J2000)	$\alpha = 9^h40^m30^s$, $\delta = 71°11'1\overset{''}{.}8$
Optical diameter at $\mu_B = 25\,mag/\Box''$	3.7 kpc × 1 kpc
Adopted extinction[b]	E_{B-V}=0.05 mag
Apparent blue luminosity	13.25 mag
Absolute blue luminosity	$-14.55\,\mathrm{mag} \,\hat{=}\, 1.0 \times 10^8 L_{B_\odot}$
Central blue surface brightness	24.47 mag/$\Box''$
Mean blue surface brightness	25.69 mag/$\Box''$
Oxygen abundance[c] $12 + \log(\frac{O}{H})$	7.7
Current star formation rate[d]	$0.004\,\mathcal{M}_\odot\,\mathrm{yr}^{-1}$

Table 3
Summarized general properties of Ho I.

[a] from the Nearby Extragalactic Database (NED)
[b] Schlegel et al. (1998)
[c] Miller & Hodge (1996)
[d] Miller & Hodge (1994)

Radius	0.85 kpc
FWHM width	1.26 kpc
H I mass	$\sim 8 \times 10^7\,\mathcal{M}_\odot$
Central H I column density	6×10^{19} cm^{-2}
Average H I column density on the rim	1.2×10^{21} cm^{-2}
Peak H I column density on the rim	2.0×10^{21} cm^{-2}
Age	80 ± 20 Myr
Energy	1.2×10^{53} erg ($\hat{=}$ 120 SNe) $\lesssim E \lesssim 2.6 \times 10^{53}$ erg ($\hat{=}$ 260 SNe)

Table 4
Properties of the central supergiant H I shell.